Available online at www.sciencedirect.com
ScienceDirect
Journal of Nuclear Materials 356 (2006) 27–49
journal of nuclear materials
www.elsevier.com/locate/jnucmat

On the effects of irradiation and helium on the yield stress changes and hardening and non-hardening embrittlement of ~8Cr tempered martensitic steels: Compilation and analysis of existing data

Takuya Yamamoto [a], G. Robert Odette [a,*], Hirotatsu Kishimoto [a], Jan-Willem Rensman [b], Pifeng Miao [a]

[a] *Department of Mechanical Engineering, University of California, Santa Barbara, CA 93106, USA*
[b] *NRG, P.O. Box 25, 1755 ZG Petten, The Netherlands*

Abstract

Data on irradiation hardening and embrittlement of 8–10Cr normalized and tempered martensitic steel (TMS) alloys has been compiled from the literature, including results from neutron, spallation proton (SP) and He-ion (HI) irradiations. Limitations of this database are briefly described. Simple, phenomenological–empirical fitting models were used to assess the dose (displacement-per-atom, dpa), irradiation temperature (T_i) and test temperature (T_t) dependence of yield stress changes ($\Delta\sigma_y$), as well as the corresponding dependence of sub-sized Charpy V-notch impact test transition temperature shifts (ΔT_c). The $\Delta\sigma_y$ are generally similar for SP and neutron irradiations, with very high and low helium to dpa ratios, respectively. Further, the $\Delta\sigma_y$ trends were found to be remarkably consistent with the T_i and dpa hardening-dependence of low alloy steels irradiated at much lower doses. The similar T_i and (low) dose dependence of $\Delta\sigma_y$ and ΔT_c, as well as an analysis of paired ΔT_c–$\Delta\sigma_y$ datasets, show that embrittlement is typically dominated by a hardening mechanism below about 400 °C. However, the corresponding hardening-Charpy shift coefficient, $C_c = \Delta T_c/\Delta\sigma_y \approx 0.38 \pm 0.18$ °C/MPa is lower than that for the fracture toughness reference temperature, T_0, with $\Delta T_0/\Delta\sigma_y \approx 0.58 \pm 0.1$ °C/MPa, indicating that sub-sized Charpy tests provide *non-conservative* estimates of embrittlement. The C_c increases at $T_i > 400$ °C, and $\Delta T_c > 0$ are sometimes observed in association with $\Delta\sigma_y \leqslant 0$, indicative of a non-hardening embrittlement (NHE) contribution. Analysis of limited data on embrittlement due to thermal aging supports this conclusion, and we hypothesize that the NHE regime may be shifted to lower temperatures by radiation enhanced diffusion. Possible effects of helium on embrittlement for T_i between 300 and 400 °C are also assessed based on observed trends in C_c. The available data is limited, scattered, and potentially confounded. However, collectively the database suggests that there is a minimal NHE due to helium up to several hundred appm. However, a contribution of helium to NHE appears to emerge at higher helium concentrations, estimated to be more than 400–600 appm. This is accompanied by a transition from transgranular cleavage (TGC) to

---

[*] Corresponding author. Tel.: +1 805 893 3525; fax: +1 805 893 8651.
E-mail address: odette@engineering.ucsb.edu (G.R. Odette).

doi:10.1016/j.jnucmat.2006.05.041

intergranular fracture (IGF). IGF generally occurs only at high $\Delta\sigma_y$. Synergistic combinations of large $\Delta\sigma_y$ and severe NHE, due to helium weakening of grain boundaries, could lead to very large transition temperature shifts in first wall and blanket structures at fusion spectrum dose levels above 50–75 dpa and in SP irradiations at much lower doses.

---

1. Introduction

An important objective for the fusion materials community is to develop a high quality database on the effects of irradiation on the constitutive and fracture properties of 8–10Cr normalized and tempered martensitic steel (TMS) alloys. This paper focuses on changes in the tensile yield stress ($\Delta\sigma_y$) and irradiation embrittlement, characterized by transition temperature shifts (ΔT_c), measured in sub-sized Charpy V-notch impact tests. A high quality database is needed to develop predictive models of the changes in $\Delta\sigma_y$ and ΔT_c (and other properties) as a function of the *combination* of all significant metallurgical and irradiation variables. The metallurgical variables include the start-of-life alloy composition (wt%), microchemistry and microstructure, including the effects of thermo-mechanical processing treatment (TMT). The primary irradiation variables include irradiation temperature (T_i) and the neutron flux (ϕ), energy spectrum [$\phi(E)$] and fluence (ϕt). The neutron irradiation variables are best represented in terms of the total and rates of production of damaging species, including displacements-per-atom (dpa), helium, hydrogen and solid transmutation products (appm). Post-irradiation testing and data analysis variables are also significant. For example, $\Delta\sigma_y$ depends on the test temperature (T_t). Ultimately a comprehensive and high quality database will be analyzed with physically based, multiscale models [1–3]. Such models will sequentially relate (a) the primary variables to microstructural evolutions; (b) the effects of these evolutions on fundamental structure-sensitive constitutive and local fracture properties; (c) and the consequences of changes in these fundamental properties to more complex engineering properties, like ΔT_c (and corresponding shifts in the fracture toughness reference temperature, ΔT_0 [1–3]). In the interim, simpler phenomenological–empirical models and physically motivated correlations will be used to analyze the growing, but imperfect database.

There have been many irradiation studies aimed at contributing to such a database. Among the most notable are the International Energy Agency (IEA) round robin project on the Japanese F82H steel [4,5], as well as the large program in Europe currently focusing on various heats of the Eurofer steel [6–8]. There are also other data based on irradiations of TMS with spallation protons (SP), which generate very high levels of helium and hydrogen [9–13]. Other pertinent data includes accelerator based ion irradiations, including with high energy He-ions (HI) [14,15]. In this paper, we summarize the preliminary results of an ongoing effort to tabulate and analyze existing $\Delta\sigma_y$ and ΔT_c data on TMS alloys. One objective is to gain a practical, working knowledge of what is required in a mechanical property database to make it functionally useful and of 'high quality'; and to assess the state of the existing data in this context. A second objective is to carry out a simple preliminary analysis to gain insight on the variables that control $\Delta\sigma_y$ and ΔT_c, including high levels of transmutation product helium.

The effects of high levels of helium under conditions of simultaneous displacement damage production and irradiation embrittlement are two of the most important issues facing the development of TMS for fusion applications. Indeed, it is largely concerns about helium that have motivated the need for the International Fusion Materials Irradiation Facility. Because of the high sink density that acts as traps, martensitic steels are generally believed to be relatively immune to helium effects [16–18]. However, at high helium levels, a significant population of bubbles forms, with number densities, sizes and spatial distributions that depend on the irradiation temperature and the alloy microstructure. The amount and distribution of helium on grain boundaries is likely to be particularly significant [19]. One school of thought has asserted that helium plays a dominant role in embrittlement [20–28], in some cases [20–22] even apparently showing a linear correlation between helium concentration and ΔT_c. A contrary view attributes a dominant role to irradiation hardening induced embrittlement, where the hardening is primarily associated with displacement damage. Thus, at least up to some concentration, helium only plays a secondary role [1,15], mainly through a direct or indirect effect on hardening. The sensitivity of hardening to helium generally appears to be modest below very high levels. However, to date it has not been possible to obtain reliable experimental assessment of helium effects on fast fracture in candidate materials at damage rates, doses and temperatures relevant to the first wall and blanket environment. Thus there has been no clear experimental resolution of this issue. Within the framework described below, we assess the issue of helium effects on fast fracture based on existing data.

Our analysis addresses several specific issues.

- The dpa, T_i, T_t (for $\Delta\sigma_y$) and metallurgical variable dependence of $\Delta\sigma_y$ and ΔT_c.
- The relation between $\Delta\sigma_y$ and ΔT_c to characterize hardening and non-hardening induced embrittlement.
- The reliability of Charpy-based ΔT_c as a surrogate for fracture toughness reference temperature (T_0) shifts (ΔT_0).
- The possible role of irradiation induced or enhanced non-hardening embrittlement (NHE) mechanisms on ΔT_c.
- The possible effect of helium on fast fracture both in terms of the local fracture mode and embrittlement shifts ΔT_c.

2. Compilation of the existing irradiation hardening and embrittlement data

Detailed descriptions of the development of a computer accessible database will be provided in the future. Most of the data is for neutron irradiations, but we also include a significant body of results of spallation proton (SP) irradiations, which generate from ≈60 to 150 appm He/dpa, as well as limited data from high energy He-ion (HI) irradiation studies implanting up to 5000 appm He. Currently, the database consists of 834 entries for $\Delta\sigma_y$ and 595 entries for ΔT_c. However, not all of the hardening and embrittlement data entries contain sufficient ancillary information to be useful in our analysis.

We first established a set of variables and parameters for each $\Delta\sigma_y$ and ΔT_c entry that are needed in a database for it to be useful. Basically, it is necessary to have comparable baseline and irradiated data and to know the details[1] of (a) the metallurgical variables, including alloy composition and TMT processing history; (b) the irradiation variables; (c) the descriptions of the test procedures and methods used to reduce, analyze and parameterize the data. Of course, it is also important to characterize uncertainties, assumptions and any possible biases in these variables, methods and parameters. There are also often complications in an experiment that are important to know, such as variations in T_i. Based on these criteria, it is necessary to conclude that the existing data generally do not yet comprise a high quality and optimally useful database. A partial list of limitations we found is as follows:

- In some cases there was incomplete and uncertain characterization of the alloy and poorly defined pairs of baseline and irradiated data sets.
- Most often there was no indication of uncertainties in key variables, that are known to often be poorly defined, or even biased, particularly T_i.
- Often there is no reported assessment of possible uncertainties or bias in the test measurements and data reduction-parameterization procedures. This is a particular issue for the ΔT_c that often were deduced from a small and, indeed, typically insufficient number of specimens.

Due to such limitations, the analysis presented below provides only a systematic, first-iteration assessment of the relations of $\Delta\sigma_y$ and ΔT_c to dpa, T_i, T_t and metallurgical variables. However, we also note that some recent datasets [8,29] on $\Delta\sigma_y$ are of much higher quality, which will be apparent in the analysis that follows. Since many different alloys have been irradiated under very different irradiation conditions, it is necessary to reduce the number of independent variables to make the analysis tractable. This is discussed in Section 3.

3. Preliminary data analysis

We first carry out an analysis involving a minimum number of independent variables. Thus it is

---

[1] Chemical composition, normalizing–tempering temperatures and times, hot/cold work strains; specimen size, geometry, orientation, test temperature, strain rate; irradiation source, dpa dose and dose rate, irradiation temperature, He and H; baseline versus post-irradiation tensile (σ_y, σ_u, σ_f, ε_u, ε_t, RA), Charpy (DBTT, USE, σ_{yd}) – all with uncertainties.

necessary first to define broad alloy categories and T_i bins to make the analysis tractable. The lumped data are naturally very scattered, but statistical fits can still be used to establish broad, common trends in $\Delta\sigma_y$ and ΔT_c as a function of dpa, T_i and T_t (for $\Delta\sigma_y$). Predicted minus measured residual plots, including those for other potential variables not included in the primary fits, can then be used to identify inaccuracies and biases in the first-iteration model. The first-iteration model can also be used to adjust the data to a common set of dpa and/or T_i conditions. We divided the alloys into four broad categories: (a) F82H; (b) Eurofer; (c) other 9CrW steels containing $9 \pm 1.5\%$ Cr and 1–2% W; and (d) 9CrMo steels containing $9 \pm 1.5\%$ Cr and $1 \pm 0.5\%$ Mo. Except at the lowest and highest irradiation temperatures, the T_i binning, described below, generally ranged from about ±15 to ±25 °C around the nominal value. These T_i bins are on the order of the corresponding irradiation temperature uncertainties. In general, the SP irradiation data have larger uncertainties in T_i. The test temperature T_t is also a very important variable. Most often the $\Delta\sigma_y$ data is reported for $T_t \approx T_i$ or $T_t \approx$ room temperature (≈23 °C), and sometimes both. The $\Delta\sigma_y$ generally decreases with increasing T_t. Thus, we analyzed available datasets to quantify this effect. However, since there is much more available data, the $\Delta\sigma_y$ results presented in this section are for nominally $T_t \approx T_i$, except for $T_i < 220$ °C, where most of the data is for $T_t \approx 23$ °C. In a few cases where only $T_t \neq T_i$ data are available, the data for $T_t \approx T_i \pm 50$ °C were also included.

3.1. Analysis of the $\Delta\sigma_y$ data [7–12,14,23,29–66]

A useful general fitting expression for $\Delta\sigma_y$ is

$$\Delta\sigma_y = \Delta\sigma_{ys}[1 - \exp(-\text{dpa}/\text{dpa}_0)]^p + \Delta\sigma_0. \quad (1)$$

Here $\Delta\sigma_{ys}$ is a saturation hardening, dpa_0 specifies the dose transient prior to saturation, and p is an effective dispersed-barrier hardening exponent. The constant hardening increment, $\Delta\sigma_0$, allows for either (a) a very rapid, but saturating, low dose hardening mechanism; or (b) a threshold dose for the initiation of hardening. The saturating form of Eq. (1) can be physically related to the depletion of solutes, in the case of a precipitation hardening mechanism, or an excluded volume type effect in the case of the accumulation of displacement damage-type defects. The initial rate of hardening is characterized by $\Delta\sigma_{ys}/\text{dpa}_0^p$.

More complex forms and detailed physical treatments could be used, but they must be based on comprehensive microstructural observations and more detailed mechanistic understanding and models than are within the scope of this initial analysis. In the case of simple dispersed barrier hardening with one type, size and strength of hardening feature, and with a number density that initially increases linearly with dose, $p \approx 1/2$. This is the so-called Makin and Minter model [30,31]. However, p may deviate from a value of 1/2 for a wide variety of reasons. These include combinations of increases in the size of a fixed number of features, size-dependent feature dislocation obstacle strength, distributions in the number, sizes and strengths of features and superposition of the various contributions to the overall strengthening. However, in view of the limitations of the present database, and the desire to make cross-comparisons between alloy classes and different T_i, we sought simplicity and consistency in the first-iteration fitting form, rather than additional complexity. Thus, we fixed a value of $p = 1/2$ and $\Delta\sigma_0 = 0$. Note that this fitting expression has the advantage that low dose data can be used to obtain estimates of the combined $k = \Delta\sigma_{ys}/\sqrt{\text{dpa}_0}$ fit parameter, even in the absence of high dose data. Thus broad trends in the $\Delta\sigma_{ys}$ and dpa_0 can then be used in such cases to derive a self-consistent model within the range of the data.

Fig. 1(a)–(g) shows plots of $\Delta\sigma_y$ versus $\sqrt{\text{dpa}}$ for T_i bins of (a) 25–220 °C (nominal 120 °C); (b) 250–280 °C (nominal 265 °C); (c) nominal 300 °C; (d) 300–360 °C (nominal 330 °C); (e) 365–390 °C (nominal 380 °C); (f) 400–440 °C (nominal 420 °C); (g) and >440 °C (nominal 500 °C) [4,7–12,14,23,29,32–66]. The black solid lines are $\Delta\sigma_y = k_\sigma\sqrt{\text{dpa}}$ fits for the low dose data (note, $k_\sigma \approx k$) and the black solid-double-dashed lines are the fits for the saturating form given in Eq. (1) with $p = 1/2$ and $\Delta\sigma_0 = 0$. In the case of neutron irradiations, different filled symbols are used to code the alloy class with circles, diamonds and squares for F82H, 9Cr–W and 9Cr–Mo alloys, respectively. The first-iteration fits are for irradiations with neutrons and SP (open symbols) and for all the alloy classes in each of the nominal T_i bins.

Fig. 1(a) shows the results for $T_i < 220$ °C. The majority of the data is for SP irradiations of 9Cr–1Mo steels, primarily from LANSCE irradiations (open symbols) with ≈150 appm He/dpa, while the partially filled diamonds show the data from SINQ irradiations with ≈60 to 83 appm He/dpa. The

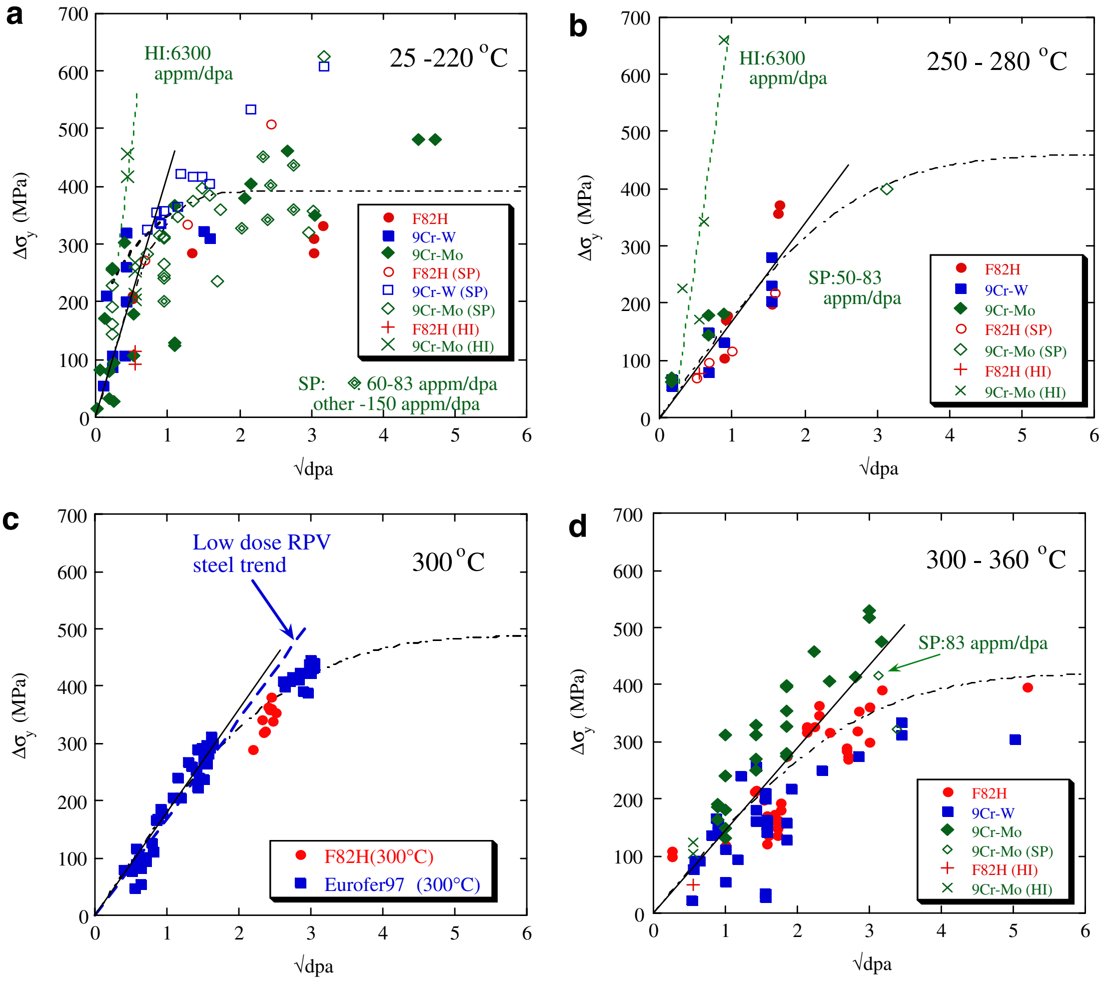

Fig. 1. The $\sqrt{}$dpa dependences of $\Delta\sigma_y$ for the temperature bins: (a) 25–220 °C (nominal 120 °C); (b) 250–280 °C (nominal 265 °C); (c) 300 °C; (d) 300–360 °C (nominal 330 °C); (e) 365–390 °C (nominal 380 °C); (f) 400–440 °C (nominal 420 °C); and (g) >440 °C (nominal 500 °C).

overall scatter bands for the SP and neutron irradiations overlap. Farrell reported that the heavy dashed line shown in Fig. 1(a), which falls near the top of the SP irradiation scatter band, provides a good fit for both the SP and neutron data for irradiations in the high flux isotope reactor for doses between ≈0.05 and 1 dpa [48]. However, most of the LANSCE $\Delta\sigma_y$ data, at the highest He/dpa, tend to fall at the top of the SP irradiation scatter band in Fig. 1(a), and hardening continues to a higher dpa in this case. Thus this may signal the onset of an effect of helium on $\Delta\sigma_y$ at very high He/dpa. But there are also a few LANSCE data points lying at the lower bound of the scatter band, and the overall mean trend of both the neutron and SP irradiation hardening data appears to be saturating at $\Delta\sigma_{ys} \approx$ 390 MPa at a low $\mathrm{dpa}_0 \approx 0.8$ dpa, albeit with very large uncertainty limits. Thus the effect of helium on hardening at low T_i remains somewhat ambiguous. The single HI irradiation $\Delta\sigma_y$ data point, with a high He/dpa ratio ≈6300 appm/dpa, falls substantially above the scatter bands for both the SP and neutron irradiations.

In the case of $T_i \approx 265$ °C, shown in Fig. 1(b), most of the data is for neutron irradiations, except of a few SP data (50–83 appm He/dpa) including the highest dose irradiations to ≈9 dpa. The latter was used to fit the saturating form for $\Delta\sigma_y$. Saturation nominally occurs at a much higher dose, with $\mathrm{dpa}_0 \approx 6.4$, than for the $T_i = 120$ °C irradiations. There does not appear to be a large and systematic difference in the $\Delta\sigma_y$ for the various alloy classes.

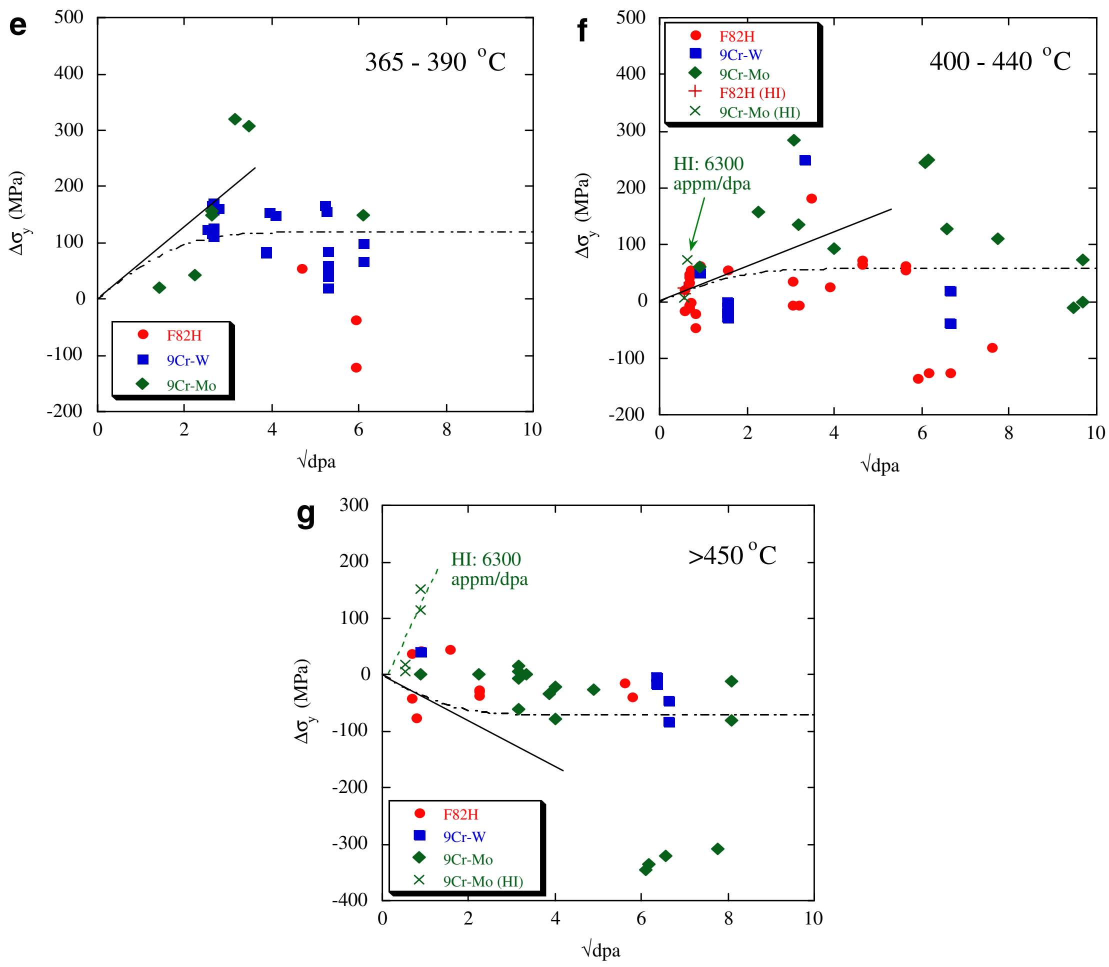

Fig. 1 (*continued*)

The nominal saturation $\Delta\sigma_{ys} \approx 460$ MPa, is actually slightly higher at 265 °C, compared to the lowest $T_i \approx 120$ °C. The hardening rate for HI irradiations is again substantially higher than for neutrons.

The data shown in Fig. 1(c) is based on a recent set of neutron irradiation $\Delta\sigma_y$ data reported by Rensman and Lucon [8,29] for a narrow range of $T_i \approx 300$ °C. The data for various T_t have been adjusted to a common value of 300 °C. The 9Cr–W data in this case are for various heats of Eurofer. Although limited to doses less than 10 dpa, the 300 °C results constitute a very high quality dataset and can be considered a lynchpin for other parts of the database and analysis. While the dose does not reach saturation levels, the data are sufficient to provide reasonable estimates for both $\Delta\sigma_{ys} \approx 490$ MPa and $\text{dpa}_0 \approx 6.8$ dpa. As shown below, the 300 °C $\Delta\sigma_{ys}$ is higher than at any other T_i, but both the $\Delta\sigma_{ys}$ and dpa_0 are reasonably consistent with extrapolations of the trends at higher and lower T_i. The heavy dashed line shows an extrapolation of the typical hardening predicted for low Cu (<0.07%) low alloy (C–Mn–Si–Mo–Ni) quenched and tempered bainitic RPV steels irradiated at ≈290 °C to a much lower maximum dpa of <0.06 dpa, is in remarkably good agreement with initial $\Delta\sigma_y$ trend for the TMS alloys in the dose range up to several dpa [67,68].

With the exception of two spallation proton irradiation data points (≈80 appm He/dpa), the $\Delta\sigma_y$ at $T_i = 330$ °C shown in Fig. 1(d) are for neutron irradiations. Note, this dataset also includes some F82H and Eurofer data at $T_i = 300$ °C previously reported by Rensman. There is an apparent trend towards saturation at a higher $\text{dpa}_0 \approx 7.7$ dpa than at both $T_i = 265$ °C and 300 °C. In general the $\Delta\sigma_y$ data for the 9Cr–1Mo alloys fall above the hardening in the F82H and 9Cr–W alloys, with the SP irradiation data lying near the lower bound of the scatter band for this steel class. In this case, the nominal saturation $\Delta\sigma_{ys} \approx 420$ MPa is lower than that for both the 265 and 300 °C irradiations.

As shown in Fig. 1(e) and (f), the data is much sparser at $T_i \geqslant 380$ °C, but, in this case, extend to a significantly higher dpa for the irradiations which were carried out in fast reactors. The $\Delta\sigma_{ys} = 119$ MPa at $T_i = 380$ °C and $=57$ MPa at 420 °C are much less than for the lower T_i. There is no low dose data in the transition in these cases to evaluate dpa$_0$. Thus we used extrapolations of the trend in $\Delta\sigma_{ys}/\sqrt{\text{dpa}_0}$ from lower T_i to estimate dpa$_0$ in this case. The $\Delta\sigma_y$ for the 9Cr–1Mo alloys are again higher than for the other steels (note, there is no F82H data at $T_i = 380$ °C). There is a tendency towards modest softening ($\Delta\sigma_y < 0$) at $T_i > 440$ °C. Much higher hardening is observed for the HI irradiations at both $T_i = 420$ and >440 °C.

Clearly, the reduced variable datasets are highly scattered. However, this is not surprising since, in addition to lumping various alloys within a broad class, there are a variety of sources of uncertainty and potential bias in the data and a range of T_i and T_t, within the various data groupings. However, in spite of the scatter, the fits can be used to establish broad trends in the database. Cross-plots of the fit parameters as functions of T_i are shown in Fig. 2. Fig. 2(a) plots the initial hardening rate coefficient $k = \Delta\sigma_{ys}/\sqrt{\text{dpa}_0}$, the $\Delta\sigma_y$ at 2 dpa and the saturation hardening, $\Delta\sigma_{ys}$. The T_i-dependence of the $\Delta\sigma_y$ parameters decreases with increasing dose below $T_i \approx 300$ °C, but remains strong at higher T_i even for $\Delta\sigma_{ys}$. The dotted-dash lines show a temperature dependence predicted by a relation

$$\Delta\sigma_y(T) = f_T(T)\Delta\sigma_y(T_r). \tag{2}$$

Here $f_T(T)$ is a function independently derived by Jones and Williams for very low dose irradiation hardening of both C–Mn ferritic and RPV bainitic steels [69]. The reference temperature, T_r, at $f_T(T_r) = 1$ is taken as 300 °C. The agreement between the predictions based on data fit for very low dose ferritic and bainitic steel irradiations and the trend for much higher dose $\Delta\sigma_y(T_i)$ data for TMS alloys is striking, and lends considerable confidence to the results of the analysis shown in Fig. 2(a). Fig. 2(b) shows the saturation dose parameter, dpa$_0$, increases systematically with increasing T_i up to ≈330 °C, and then *apparently* decreases at higher T_i. Due to the paucity and scatter in the data, however, the estimates of $\Delta\sigma_{ys}$ (at lower T_i) and dpa$_0$ (at higher T_i), are very uncertain, indicating the need for additional data. Nevertheless the average trends are systematic and reasonably self-consistent compared to interpolations at T_i both above and below 350 °C.

As noted above, Rensman has suggested that the effect of test temperature can also be treated by a dose-independent adjustment factor, $g(T_t) = \Delta\sigma_y(T_t)/\Delta\sigma_y(25\ °\text{C})$ that he derived from his

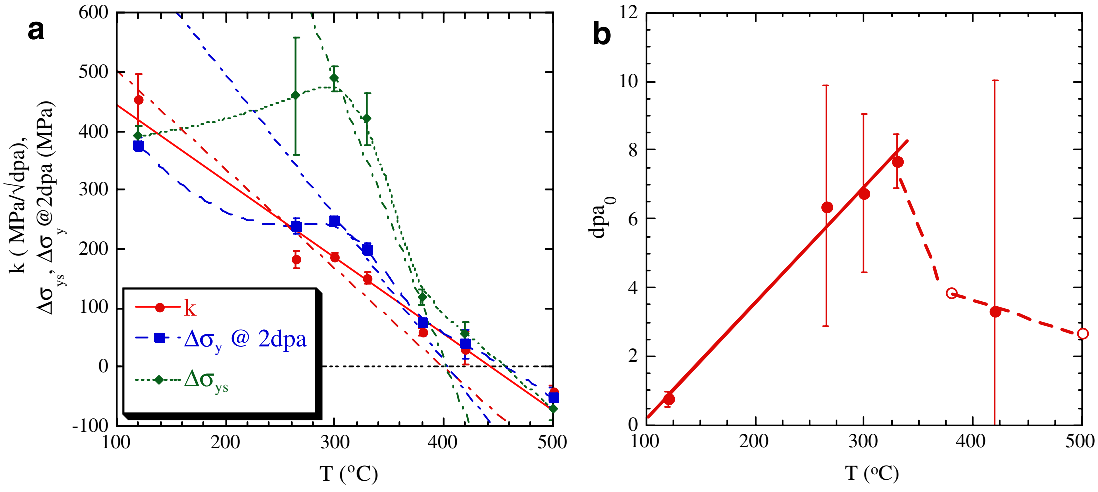

Fig. 2. (a) The T_i dependence of the initial hardening rate, $k = \Delta\sigma_{ys}/\sqrt{\text{dpa}_0}$ (MPa/$\sqrt{\text{dpa}}$), hardening at 2 dpa, and the saturation hardening, $\Delta\sigma_{ys}$, evaluated from the fits to the data shown in Fig. 1(a)–(g). The corresponding f_T functions from Jones and Williams [69] normalized at 300 °C are also shown as the dotted-dash lines; (b) The T_i dependence of the dpa$_0$. The values for the three higher temperatures (open symbols) were estimated by combining a linear fit of the k data points shown in (a) and $\Delta\sigma_{ys}$.

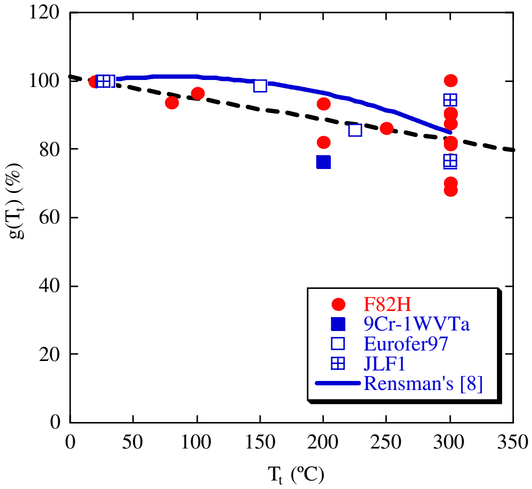

Fig. 3. The $g(T_t)$ (solid line) from Rensman and fit to the UCSB $\sigma_y(T_t)/\Delta\sigma_y(25\ °\mathrm{C})$ database (dashed line).

$T_i \approx 300\ °\mathrm{C}$ database [8]. This $g(T_t)$, is shown in Fig. 3 along with the corresponding $g(T_t)$ for sets of $\Delta\sigma_y(T_t)$ in our database for $250 \leqslant T_i \leqslant 300\ °\mathrm{C}$. The data are restricted to $T_t \leqslant T_i + 50\ °\mathrm{C}$ to avoid excessive damage annealing. The results scatter around the Rensman's $g(T_t)$ but yield a similar mean trend shown by the dashed least squares fit line. Note that Rensman also found that $g(T_t)$ shows a larger decrease in $\Delta\sigma_y$ with increasing T_t for lower $T_i \approx 60\ °\mathrm{C}$, which is probably due to annealing effects.

Fig. 2 constitutes a first-iteration model for $\Delta\sigma_y(\mathrm{dpa}, T_i)$ for $T_i \approx T_t$. Fig. 4 shows model predictions of $\Delta\sigma_y(\mathrm{dpa})$ created for $T_i = T_t$ from 200 to 500 °C using linear regression of $k(T_i)$ and interpolation of $\Delta\sigma_{ys}$. The $\Delta\sigma_y(\mathrm{dpa}, T_i)$ model expression between the actual and nominal T_i can be used to adjust the individual data to a common set of conditions. The results of adjusting the $\Delta\sigma_y$ for the irradiations between $T_i \approx 250$ and 360 °C to a common $T_i = T_t = 300\ °\mathrm{C}$ are shown in Fig. 5. While there is considerable scatter, primarily due to uncertainties in T_i, clear separation of the data by the alloy group is observed. Eq. (1) can be fit to the individual alloy subsets of data. The $\mathrm{dpa}_0/\sigma_{ys}$ (dpa/MPa) are $7.7 \pm 2.7/431 \pm 53$, $5.4 \pm 1.7/395 \pm 68$, $10.2 \pm 4.6/590 \pm 62$ and $7.2 \pm 0.9/510 \pm 22$, for F82H, 9CrW, 9CrMo and Eurofer97, respectively. The standard deviation between the measured and predicted values is $\approx$59, 55, 57 and 22 MPa for F82H, 9CrW, 9CrMo and Eurofer97, respectively. The limited SP irradiation $\Delta\sigma_y$ for F82H follows the neutron irradiation trends while those for 9CrMo appear to fall below the fitted trend, but this may be due to the fact that those specimens were irradiated $\approx$50 °C higher temperature for the last 15% of the dose [10]. Further refinement of the model, in part based on analysis of the residuals, will be carried out in the future.

In summary, irradiation hardening can be described by a saturating function of the $\sqrt{\mathrm{dpa}}$ that is characterized by a saturation hardening, $\Delta\sigma_{ys}$, and a saturation dose parameter, dpa_0. The $\Delta\sigma_{ys}$ peaks at $\approx$490 MPa at $T_i \approx 300\ °\mathrm{C}$, with a weak dependence at lower T_i at less than $\approx$300 °C. However, $\Delta\sigma_{ys}$ decreases rapidly at higher temperatures,

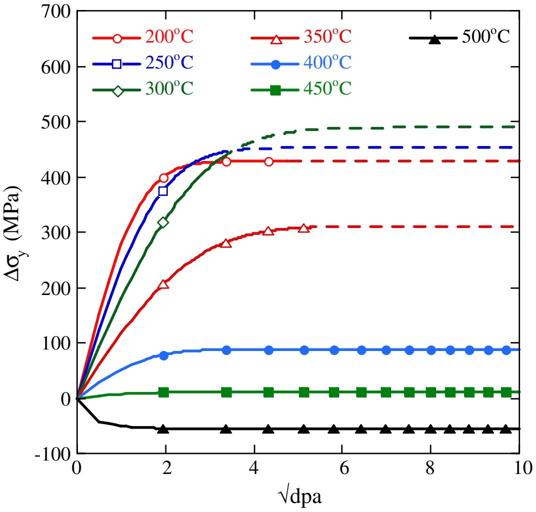

Fig. 4. Generic model predictions of $\Delta\sigma_y(\mathrm{dpa})$ for $T_i = T_t$ from 200 to 500 °C.

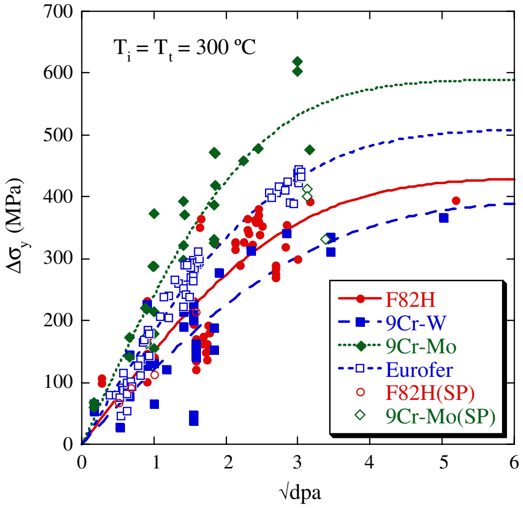

Fig. 5. The $\Delta\sigma_y$–$\sqrt{\mathrm{dpa}}$ data adjusted to common $T_i = T_t = 300\ °\mathrm{C}$ along with fits for the different alloy classes.

with softening observed at $T_i > 440$ °C. The saturation dose parameter, dpa_0, increases up to ≈330 °C, but also appears to decrease at higher T_i. The low dose hardening trends at ≈300 °C in the TMS alloys are remarkably similar to those observed in much lower dose irradiations of ferritic (C–Mn–Si) and low alloy (C–Mn–Si–Mo–Ni) bainitic RPV steels. The SP $\Delta\sigma_y$ are similar to or slightly less than for neutron irradiations, at least for T_i between 250 and 360 °C. The $\Delta\sigma_y$ also decreases with increasing T_t, in a way that can be approximately accounted for with the adjustment factor shown in Fig. 3, and can be primarily ascribed to the corresponding change in the shear modulus. Finally, there are systematic differences in the $\Delta\sigma_y$ trends observed for the various alloy classes that will be assessed in more detail in the future. Note a number of these trends were also identified in a neural network analysis of the database.

In closing we add one important caveat to this analysis. Specifically, the dpa range is limited to relatively low doses, especially for data at $T_i \leqslant 380$ °C. Thus these results should be revised as additional data becomes available, and extreme caution should be applied in extrapolating the results to higher dpa, where high dose softening has been reported at $T_i \approx 400$ °C [65], as well as general softening for higher $T_i \geqslant 430$ °C [32,39,41,43,58,70,71].

3.2. Framework to assess various embrittlement mechanisms

In this section we describe the framework to better assess several different mechanisms of irradiation embrittlement, including irradiation hardening and various non-hardening embrittlement (NHE) processes. It is noted that this framework has been used to design a series of experiments that are being conducted as part of the US–Japan collaborative irradiation program in the high flux isotope reactor (HFIR).

1. 'Brittle' fracture occurs in bcc alloys when the elevated normal stress ($\sigma_n = M\sigma_y$) in front of a notch or crack tip exceeds a critical local fracture stress for transgranular cleavage (σ_c^*) or intergranular (σ_{ig}^*) fracture over a critical microstructural volume of material (V^*), or $\sigma_n(V^*) \geqslant \sigma_c^*$. Here, σ_y is the yield stress and M is a constraint factor that varies between about 2 and 4 depending on the notch/crack geometry and the alloy strain-hardening rate [1,72,73].
2. At low irradiation temperatures (< ≈ 375–400 °C), and in the absence of high levels of helium embrittlement, (ΔT_c) is due to irradiation hardening and can be correlated with changes in yield stress ($\Delta\sigma_y$), as $\Delta T_c = C_c\Delta\sigma_y$ [1,15,72,73]. For Charpy impact tests. the value of the hardening-embrittlement coefficient C_c depends on both $\Delta\sigma_y$ and the elastic cleavage transition temperature and upper shelf energy of a particular unirradiated alloy [72].
3. As has been shown above, at high irradiation temperatures (> ≈ 440 °C) there is typically either little or no hardening, or even some degree of softening, with $\Delta\sigma_y \leqslant 0$. However, positive ΔT_c may occur in this temperature regime as the result of reductions in σ^* due to irradiation enhanced thermal aging processes [1]. Such NHE processes include precipitation or coarsening of brittle phases, grain boundary segregation of solutes, such as phosphorous, and instabilities in the tempered martensitic substructure [1,24,74,75]. In 8–10Cr martensitic steels containing significant quantities of tungsten, a primary non-hardening embrittlement mechanism is precipitation of brittle Laves phases on prior austenitic grain boundaries (PAGs). Purely thermal NHE occurs at ≈500 °C and above; but it appears that radiation enhanced diffusion decreases the lower leg of the time–temperature NHE C-curve to about 400 °C or less [1]. This is a concern, since combinations of $\Delta\sigma_y$ and NHE may give rise to very large ΔT_c. Significant NHE is signaled by large, or alternatively, negative (when $\Delta T > 0$ and $\Delta\sigma_y < 0$) values of C_c and often, a transition from transgranular cleavage (TGC) to intergranular fracture (IGF).
4. The accumulation of helium and hydrogen on PAGs may also lead to NHE. We will focus on the potential effect of large amounts of helium on NHE, but in some cases this may be difficult to distinguished from a corresponding high concentration of hydrogen. The distribution of helium on the grain boundaries is critical. For example, a coarse distribution of large bubbles would be expected to have a modest effect on ΔT_c, while a monolayer-type film of boundary would likely be most damaging [1].
5. As noted above, NHE mechanisms are generally associated with a transition from a TGC to IG local fracture mode. While oversimplified, a conceptual model of the competing effects TGC

versus IGF is very useful. The model posits that the TGC continues to be the fracture path of least resistance as long as it has a lower critical stress than that for IGF. Thus, gradual weakening of the PAGs by helium (and/or other mechanisms) would not be reflected in IGF until σ^*_{ig} falls below σ^*_{c}, where ΔT_{c} depends synergistically on both $\sigma^*_{\mathrm{ig}} - \sigma^*_{\mathrm{c}}$ (<0) and $\Delta\sigma_{\mathrm{y}}$. Of course in reality the transition would not be abrupt and the conceptual model is oversimplified.

6. High levels of helium may also contribute an increment of hardening beyond that due to displacement damage alone. However, as noted previously, the incremental hardening appears to be modest up to fairly high concentration [9,10,16,76], at least at lower irradiation temperatures.
7. A number of experimental studies have used nickel doping to produce high concentrations of helium by two-stage $^{58}\mathrm{Ni}(n_{\mathrm{th}},\gamma)\!-\!>{}^{59}\mathrm{Ni}(n_{\mathrm{th}},\alpha)$ reactions. It is well established that nickel additions result in additional hardening at lower irradiation temperatures [33,77–79]. This may be due to enhancement of hardening from defect clusters as well as fine scale nickel enriched precipitates [80,81]. More generally, nickel additions change the transformation temperatures and kinetics in quenched and tempered steels, hence, modifying the overall microstructure. Thus increases in ΔT_{c} associated with nickel doping may, or may not, be due to helium.
8. Doping with boron isotopes (natural boron is $\approx$0.2 ^{10}B and 0.8 ^{11}B) can also be used to produce large quantities of helium from the $^{10}\mathrm{B}(n,\alpha)^{6}\mathrm{Li}$ thermal neutron reaction. However, the solubility of boron in steels is extremely low, and boron doping is also confounded by (a) the non-uniform distributions, which tend to segregate boron at PAGs and other interfaces and/or to form boride precipitate phases; (b) boron's general effects on the microstructure and properties of quenched and tempered alloys; (c) boron's role in strengthening grain boundaries; (d) the production of equal amounts of transmutant lithium and helium while eliminating boron; (e) very rapid transmutation and burn-out of boron at relatively low dpa; and, (f) at low doses, excess dpa due to recoils from the boron n, α reactions.
9. The effects of such confounding factors can be partially mitigated by careful experimental designs. For example, comparisons of ΔT in paired alloys doped with either ^{58}Ni or ^{60}Ni (alternatively ^{10}B or ^{11}B) can help isolate the independent effect of helium.

Within this framework the next section evaluates the relation between ΔT_{c} and dpa and between ΔT_{c} and $\Delta\sigma_{\mathrm{y}}$. The $\Delta T_{\mathrm{c}}/\Delta\sigma_{\mathrm{y}}$ relation is then used to assess the contributions of NHE, including potential effects of high levels of He.

3.3. Preliminary analysis of the ΔT_c data

We carried out a similar analysis of ΔT_{c} as a function of dpa and T_{i}. However, in this case, the alloy classes were analyzed separately, since there were more significant differences between the various steels and a common T_{i} binning was not as useful. The data, which in most cases were very scattered, could be reasonably fit using a simpler non-saturating function

$$\Delta T_{\mathrm{c}} = k_{\mathrm{c}}\sqrt{\mathrm{dpa}}. \tag{3}$$

The ΔT_{c} versus $\sqrt{}$dpa data and k_{c} fits are shown in Fig. 6(a)–(c) [4,7,20,22,26,27,50–58,82–96]. Note, these plots do not include a comprehensive database assembled by Schneider and co-workers [93,94] on a variety of $\approx$9Cr–W and $\approx$9Cr–Mo steels, including some alloys with Ni additions, as well as F82H. This database will be discussed further below. Fig. 7 shows a cross-plot of k_{c} from the fits in Fig. 6 as a function of T_{i}. The 9Cr–Mo and F82H alloys show the lowest and highest k_{c}, respectively, with the 9Cr–W steels generally falling between, but closer to F82H. The T_{i} dependence of the k_{c} is in reasonable agreement with the corresponding T_{i}-dependence of the initial irradiation hardening as shown by the various solid and dashed lines in Fig. 7 that are $\Delta\sigma_{\mathrm{y}}(2\mathrm{dpa})/\sqrt{2}$ multiplied by $\Delta T_{\mathrm{c}}/\Delta\sigma_{\mathrm{y}}$ conversion factors of = 0.18, 0.30 and 0.38 °C/MPa for the 9Cr–Mo, 9Cr–W and F82H, respectively. Notably, these values of $\Delta T_{\mathrm{c}}/\Delta\sigma_{\mathrm{y}}$ are much less than the $\Delta T_0/\Delta\sigma_{\mathrm{y}} \approx 0.58 \pm 0.1$ °C/MPa found for fracture toughness reference temperature shifts [1]. In the case of F82H, a significant ΔT_{c} persists in the $T_{\mathrm{i}} > 400$ °C, when irradiation hardening is minimal, or when softening is observed. Note that high, and even negative values, of $\Delta T_{\mathrm{c}}/\Delta\sigma_{\mathrm{y}}$ are also observed in the Schneider's database for $T_{\mathrm{i}} = 450$ °C.

Fig. 8 plots the available paired ΔT_{c} and $\Delta\sigma_{\mathrm{y}}$ datasets, including results from the preliminary assessment of Schneider's database. In the latter case, the $\Delta\sigma_{\mathrm{y}}$ is based on measurements of changes in dynamic yield stress. Fig. 8(a) shows the results

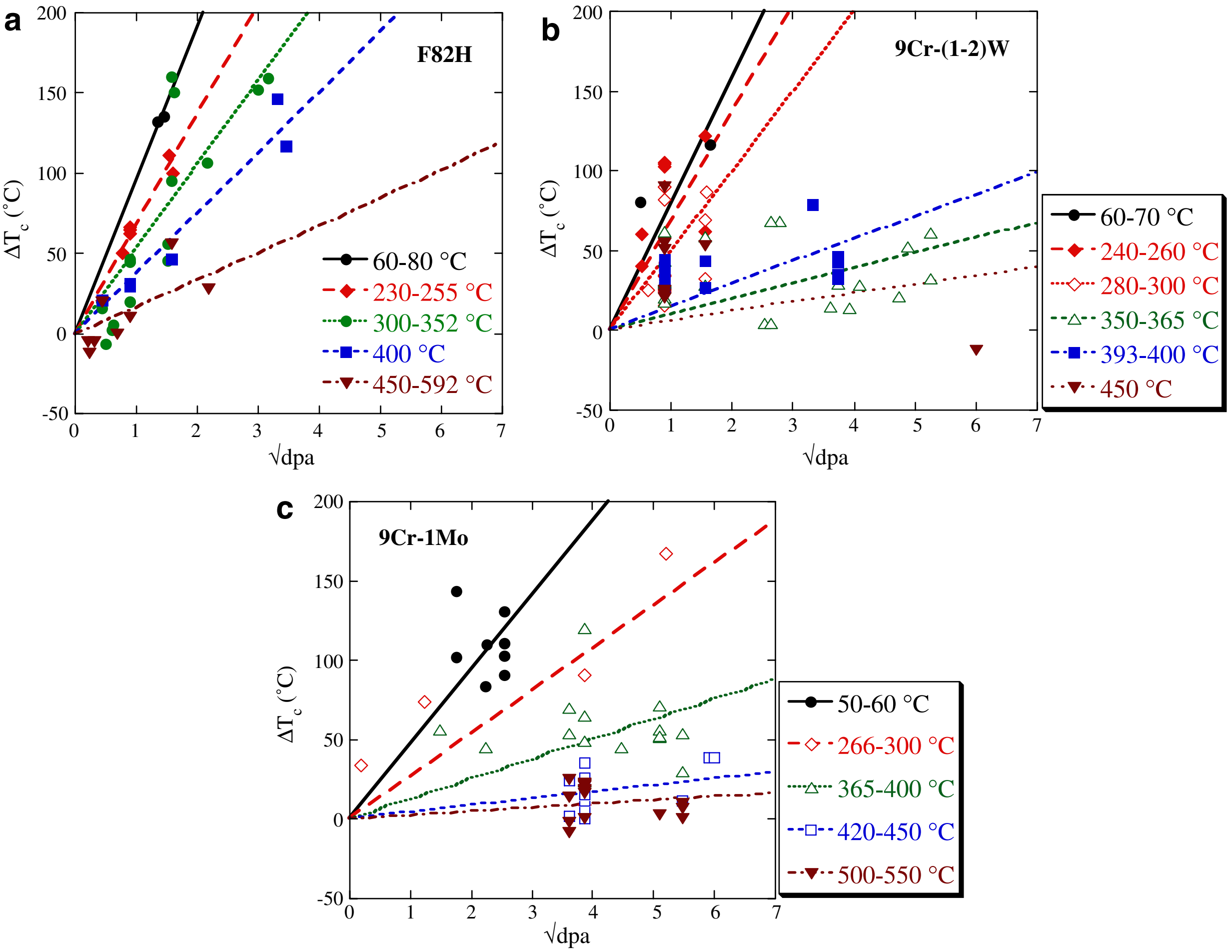

Fig. 6. The $\sqrt{\text{dpa}}$ dependence of ΔT_c for (a) F82H; (b) 9Cr–W; and (c) 9Cr–Mo steels and corresponding fits at various T_i.

for $T_i < 400$ and Fig. 8(b) is for $400 \leqslant T_i \leqslant 450$ °C. Where possible, the $\Delta\sigma_y$ are for $T_t = 25$ °C. However, the $T_t = 25$ °C data is limited for static tensile test measurements of $\Delta\sigma_y$, and the open symbols are for cases when only $T_t \approx T_i$ are available. The lines show the nominal and ± one standard deviations fits for static tensile data only. Note the data with $\Delta\sigma_y < 0$ are not used in these fits. Once again, the data are highly scattered. The fitted $\Delta T_c/\Delta\sigma_y$ are $\approx 0.38 \pm 0.18$ °C/MPa for $T_i < 400$ and 0.76 ± 0.42 °C/MPa for $400 \leqslant T_i \leqslant 450$ °C bin. Schneider's database also showed similar trends with $\Delta T_c/\Delta\sigma_y \approx 0.41 \pm 0.17$ °C/MPa for $T_i < 400$ and 0.75 ± 1.07 °C/MPa for $T_i \geqslant 400$ °C bin. Fig. 9 shows the $\Delta T_c/\Delta\sigma_y$ as function of T_i, where the static and dynamic (d) $\Delta T_c/\Delta\sigma_{y/yd}$ were averaged over the various Charpy T_i-bins. Error bars show the standard deviation in each T_i bin. Both static and dynamic $\Delta T_c/\Delta\sigma_y$ are ≈0.4 up to $T_i \approx 360$ °C, increasing to >1 °C/MPa with very large scatter at $T_i = 450$. These trends are consistent with those observed for F82H and the 9Cr–W steels in Fig. 6, showing that $\Delta T_c/\sqrt{\text{dpa}}$ persists above 400 °C when $\Delta\sigma_y$ is ≈0, or is even <0.

These results lead to two very important conclusions:

- The $\Delta T_c/\Delta\sigma_y$ irradiations at $T_i < 400$ °C are generally less than the corresponding fracture toughness indexed $\Delta T_0/\Delta\sigma_y$ shifts. Thus the ΔT_c from sub-sized Charpy tests are probably non-conservative, and may seriously underestimate the embrittlement potential of TMS alloys. Assuming a nominal $\Delta T_0/\Delta\sigma_y \approx 0.6 \pm 0.1$ °C/MPa and a maximum $\Delta\sigma_y = 600$ MPa leads to an estimated $\Delta T_0 \approx 360 \pm 60$ °C. Later we will show that the $\Delta T_c/\Delta\sigma_y$, hence presumably $\Delta T_0/\Delta\sigma_y$ as well, may be even larger for steels containing

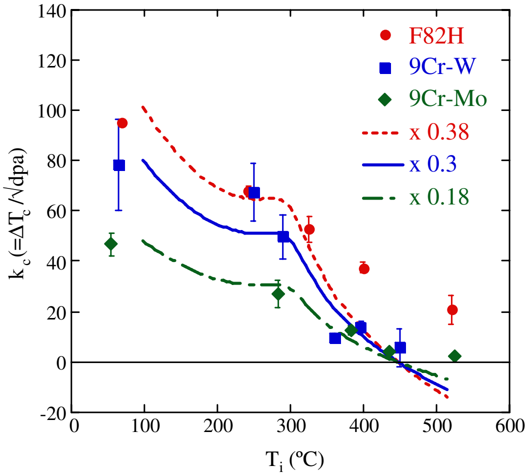

Fig. 7. The symbols are the $k_c(=\Delta T_c/\sqrt{\text{dpa}})$ versus T_i, found from the fits to the data for the various alloy groups shown in Fig. 6. The dashed lines represent the average $\Delta\sigma_y$ (2 dpa, T_i) derived from the data in Fig. 1 multiplied by an alloy class dependent C_c shown in the legend.

high levels of helium, which would likely result in unacceptable T_0 values.

- The $\Delta T_c/\Delta\sigma_y$ are larger for irradiations at $T_i \geqslant 400$ °C; and in some cases $\Delta T_c > 0$ for $\Delta\sigma_y < 0$, indicating a contribution of NHE.

3.4. Non-hardening embrittlement

The persistence of ΔT_c to higher temperatures and large or negative values of $\Delta T_c/\Delta\sigma_y$ signal a non-hardening embrittlement (NHE) contribution. There are several potential sources of NHE that occur primarily at higher temperatures under thermal aging conditions, including some that may also be assisted by irradiation:

- Precipitation (Laves) and coarsening (carbides) of brittle grain boundary phases that act as cleavage 'trigger-particle' or brittle grain boundary fracture paths.
- Grain boundary segregation of trace impurities, such as P, and/or depletion of beneficial elements like C.
- Instabilities in the dislocation and lath-packet substructures leading to larger effective subgrain sizes.
- Development of damage, particularly on grain boundaries, in the form of microcracks, gas bubbles and creep cavities. The potential for NHE by high concentrations of helium is discussed below.
- In principle, high concentrations of transmutant hydrogen may also be a potential source of embrittlement in TMS. Hydrogen embrittlement is enhanced by high strength levels, hence, may act synergistically with irradiation hardening. Hydrogen is associated with the reduced cohesion of grain boundaries, where it is segregates to much higher concentrations than in the bulk, hence may also interact with other NHE mechanisms, including those due to helium (see below). However, there are no systematic studies of the effects of hydrogen embrittlement in TMS, except

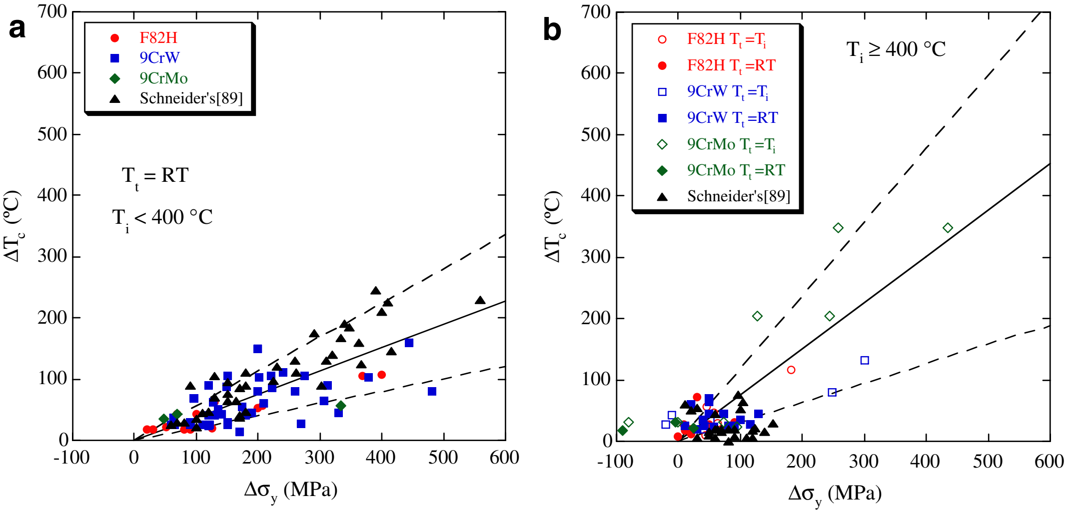

Fig. 8. ΔT_c versus $\Delta\sigma_y$ (or equivalent) plots from paired datasets from (a) $T_i < 400$ and (b) $T_i \geqslant 400$ °C.

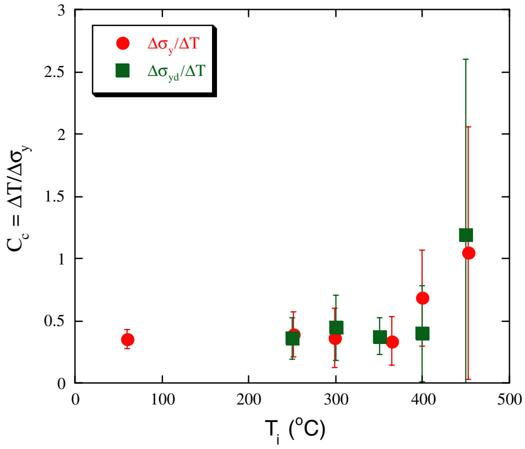

Fig. 9. Static and dynamic (designated by the subscript d) $\Delta T_c/\Delta\sigma_{y/yd}$ versus T_i averaged over the various T_i-bins. The error bars show the standard deviation in each T_i bin.

at low temperatures following charging [97]. Post-irradiation thermal desorption studies, including some H-ion implantation experiments, suggest that most of the hydrogen is expected to diffuse out at $T_i \geqslant 250$ °C [16,98].

NHE due to precipitation and solute segregation can result from radiation-enhanced diffusion (RED) and radiation induced segregation (RIS). Further, excess fluxes of point defects enhance structural instabilities, like dislocation recovery. In particular, it is expected that the diffusion controlled, lower leg of a time–temperature ΔT_c C-curve is shifted to lower temperatures by RED as is illustrated in Fig. 10. The T_i corresponding to a bulk RED coefficient (D^*) under irradiation that is the same as the thermal diffusion coefficient (D_{th}) at the higher aging temperature T_a can be estimated from

$$T_i = T_a\{1 - [RT_u/Q_d]\ln(r)\}. \tag{4}$$

Here Q_d is activation energy for thermal diffusion and r is the D^*/D_{th} ratio at T_i. Assuming a reasonable value of $r = 10^4$ at a dose rate of 3×10^{-7} dpa/s and $Q_d = 300$ kJ/mole, Eq. (4) predicts a $T_i \approx 405$ °C for $T_a = 600$ °C. The NHE kinetics would be further accelerated if irradiation enhances other rate limiting steps like precipitate nucleation or dissolution. Note, however, the effects of RED on grain boundary dominated transport processes are likely to be less significant and have not been modeled. Further, NHE associated with RED processes like precipitation are bounded by factors such as solute depletion, or may transform to slower kinetics, like coarsening versus growth of a brittle phase.

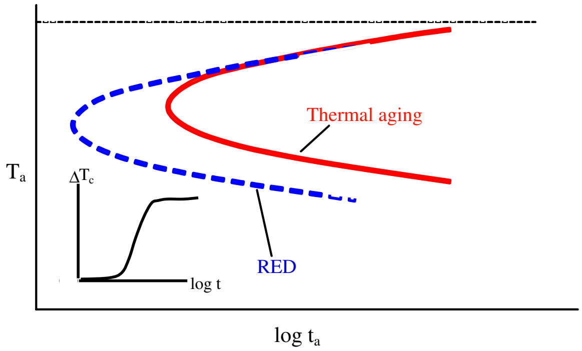

Fig. 10. Schematic illustration of the effect of radiation enhanced diffusion (RED) on time–temperature ΔT_c embrittlement C-curves.

The limited data on thermal embrittlement of TMS alloys [24,25,74,75,99] is summarized in Fig. 11 as ΔT_c versus t_a plots for various alloys and T_a. Notably, significant ΔT_c are observed for aging $t_a \leqslant 10000$ h in the T_a range from 500 to 650 °C. As expected, ΔT_c increases with t_a and T_a. The apparently linear increase with t_a and the rather modest T_a-dependence are not understood. This NHE due to thermal aging is probably primarily due to precipitation of brittle Laves (nominally Fe_2W) phases on the grain boundaries. Thus, as expected, the alloy JLS-2 with 3% W has a somewhat larger ΔT_c compared to F82H with 2% W. The legend in Fig. 11 also shows the equivalent temperature under RED conditions based on Eq. (4) and the parameters cited above.

Fig. 12 plots an embrittlement time (or inverse rate) parameter $\ln(t_a/\Delta T_c)$ versus T_a for the F82H TMS alloy. The dashed line shows the prediction of Eq. (4) and associated parameters for the effect of RED. The open diamonds show the corresponding embrittlement rate for the irradiated data shown in Fig. 7 at ≈400 and 510 °C for a dpa rate of 3.5×10^{-7}/s (≈10 dpa/year). The NHE data in Fig. 12 is in reasonable agreement with the predicted effect of RED, but has a temperature-dependence that is opposite to that predicted by the simple model. In part, this may be due to ignoring a contribution to ΔT_c from irradiation hardening at 400 °C and a possible softening effect at ≈500 °C. However, these results do indicate that significant ΔT_c associated with irradiation enhanced

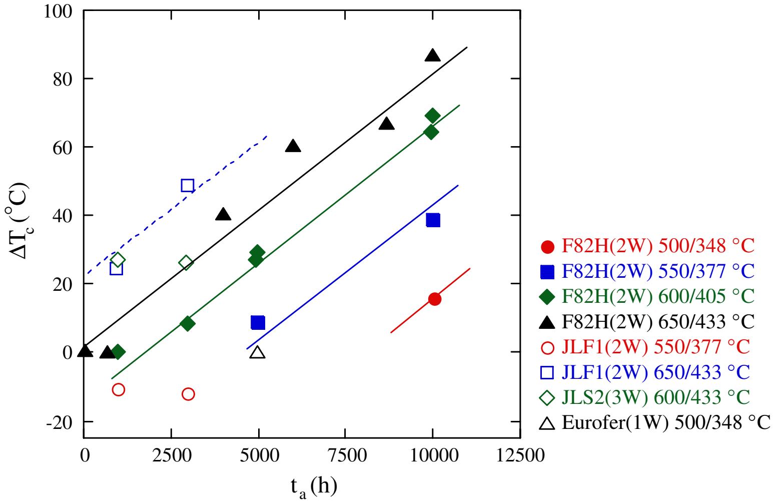

Fig. 11. The ΔT_c versus aging time t_a and temperature, T_a. The second set of entries in the figure caption are estimates of the equivalent temperatures accounting for RED, assuming a dose rate of 3×10^{-7} dpa/s and $Q_d = 300$ kJ/mole (see text for details).

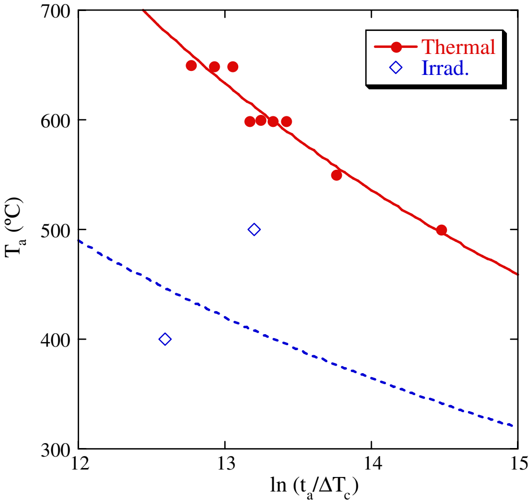

Fig. 12. An embrittlement rate parameter, $\ln(t_a/\Delta T_c)$, versus T_a for F82H. The dashed line shows the prediction of Eq. (4) and associated parameters estimating the effect of RED. The symbols show the corresponding embrittlement rate for the irradiated data shown in Fig. 7 at ≈400 and 510 °C assuming a dpa rate of 3.5×10^{-7}/s (≈10 dpa/year).

NHE processes can be expected at $T_i > 400$ °C. While such NHE may or may not itself be a major problem, it will likely interact synergistically with other hardening and NHE mechanisms, thus potentially producing a significant contribution to ΔT_c.

NHE is often accompanied by a transition from transgranular cleavage fracture (TGC) to intergranular fracture (IGF) along weakened PAGs or other boundaries. As discussed elsewhere [1], the transition to IGF can be conceptually linked to gradual decrease of a critical grain boundary fracture stress σ^*_{ig} to the point where it falls below the critical stress, σ^*_c, for TGF. Developing an IGF ΔT_c model is an important future objective.

3.5. He effects on fast fracture and embrittlement

Since the effects of fusion relevant helium levels on hardening appear to be modest, the major issue is the potential role of helium in NHE. The framework outlined above has been incorporated in recent experiments. For example, a single variable experiment is being carried out to compare the ΔT_0, $\Delta\sigma_y$ and C_k for TMS doped with ^{58}Ni and ^{60}Ni isotopes as well as natural Ni; and another experiment is planned that will use alloys doped with ^{10}B and ^{11}B isotopes. However, these principles are generally not reflected in past studies. Indeed, most previous experiments did not even include tensile specimens to provide $\Delta\sigma_y$ data as a complement to the ΔT_c measurements from sub-sized Charpy tests; and even the simple expedient of microhardness measurements to estimate irradiation hardening was rarely exploited. Further, there have been relatively few fractographic studies to characterize the local fracture mode, and any transitions from TGC to IGF in irradiated alloys as a function of helium content.

Nevertheless, it is still possible to analyze existing data to try to detect, and even quantitatively estimate, the potential helium NHE by examining the relation between ΔT_c and $\Delta\sigma_y$ and/or $C_c = \Delta T_c/\Delta\sigma_y$. Large increases in C_c with increasing helium signal a NHE helium contribution and vice versa. Of course, even if C_c appears to increase with helium, a corresponding NHE is not assured due to the confounding factors. Further, uncertainties in C_c must also be considered. Even relatively optimistic estimates of uncertainties of only ±10 °C in ΔT_c and ± 20 MPa in $\Delta\sigma_y$ mean uncertainties in C_c of $\approx \pm 10/\Delta T_c$ (°C/MPa) for an actual $C_c = 0.4$ °C/MPa. Thus a relatively large scatter in C_c values should be entirely anticipated, particularly at small ΔT_c, and it is always useful to examine ΔT versus $\Delta\sigma_y$ scatter plots as well as the trends in C_c. Of course there are other indicators of helium to NHE. The most significant is the transition from TGC to IGF above some critical level of helium [10,12,16].

There are pertinent data from spallation proton irradiations based on the so-called small punch tests (sp) that can be used to estimate both irradiation hardening and transition temperature shifts [12,13]. However, the small punch technique is not a true fracture test per se. An effective yield stress (σ_{yp}) and corresponding irradiation hardening ($\Delta\sigma_{yp}$) are evaluated based on the nonlinearities in punch load–displacement curves. An effective transition temperature (T_{sp}) and corresponding irradiation induced shifts (ΔT_{sp}) are determined by plotting the integrated load–displacement energy at fracture, measured at the point of a large load drop, as a function of the test temperature. Since small punch tests inherently involve static, low constraint conditions, with small values of M (or ratios of the maximum principal stress relative to the σ_y), the brittle (TGC or IGF) to ductile transition, if any, occurs at temperatures that are much lower than for standard, and even sub-sized, Charpy impact tests; and the corresponding shifts in ΔT_{sp}, due to irradiation embrittlement, are also much lower than ΔT_c. An empirical adjustment of $\Delta T_c^{(sp)} \approx 2.5\Delta T_{sp}$ is used here to evaluate $\Delta T_c^{(sp)}$ and C_c [12,13,15,100,101]. Finally, while highly unusual in steels, brittle fracture may also occur in tensile tests with lower bound values of $M \approx 1$. As noted above this implies a very low value of the critical brittle fracture stress. However, even in a tensile test, M is somewhat greater than 1 in the necked region beyond the uniform strain limit. The maximum M increases with necking, and can be related to the reduction in area at fracture and the corresponding tri-axial stress state in the necked region.

Fig. 13(a) and (b) summarizes the very limited available Charpy-tensile test ΔT_c versus $\Delta\sigma_y$ data with helium variations in nominally similar alloys with and without nickel or boron doping for irradiations at ≈300 and 400 °C, respectively [26,52,55,56,82,87,91,102]. Helium content shown in parenthesis is common for both Charpy and tensile specimens except for some cases where data for a common condition are not available; in these cases, both values of (Charpy/tensile) specimens are shown. The dashed lines indicate the scatter in the general database for ΔT_c versus $\Delta\sigma_y$. Two data sets are for a 9CrMo alloy both undoped and doped with 2% Ni irradiated at 300 and 400 °C. The nickel doping results in increases in helium from ≈14 to 234 and 33 to 369 appm in these two cases, respectively. Both the doped and undoped alloys fall on virtually the same ΔT_c versus $\Delta\sigma_y$ line with $C_c \approx 0.40$ °C/MPa at 300 °C and $C_c \approx 0.82$ °C/MPa at 400 °C. Thus while the nickel addition increases the $\Delta\sigma_y$ in both these cases, there is no independent NHE effect of either nickel, or helium, indicated by this data set. The corresponding ΔT_c for a 9Cr2W alloy doped with 2% nickel irradiated at ≈300 °C with ≈115 appm He falls slightly above the ΔT_c versus $\Delta\sigma_y$ line for the corresponding undoped steel with ≈5 appm helium, with C_c of 0.44 and 0.32 °C/MPa, respectively. However, both are well within the overall ΔT_c versus $\Delta\sigma_y$ and C_c scatter band. A generally similar result is found for natural B doped F82H and JLF1 steels irradiated at 300 °C, with ≈23–40 appm He, compared to undoped alloys with ≈3 appm He. These results may suggest a slightly stronger effect of boron compared to nickel doping, with values of ≈0.53 and 0.75 (high helium) versus 0.43 and 0.58 (low helium), respectively.

The ΔT_c versus $\Delta\sigma_y$ for the 12Cr1Mo Ni-doped and undoped alloys in Fig. 13(a) and (b) also show no effect of helium and the data all fall within the normal scatter bands [26,91,102]. However, a recent review paper included 300 °C data on F82H doped with various isotopes of B showed a systematic increase of C_c with increasing helium up to 340 appm [103]. Thus these results may also suggest a stronger effect of boron compared to nickel doping, perhaps due to B segregation to PAGs. Overall, however, the limited nickel and boron doping data show little effect of helium on C_c up to concentrations ≈350 appm.

Dai and co-workers have reported a nearly linear correlation between the helium level and ΔT_{sp} for

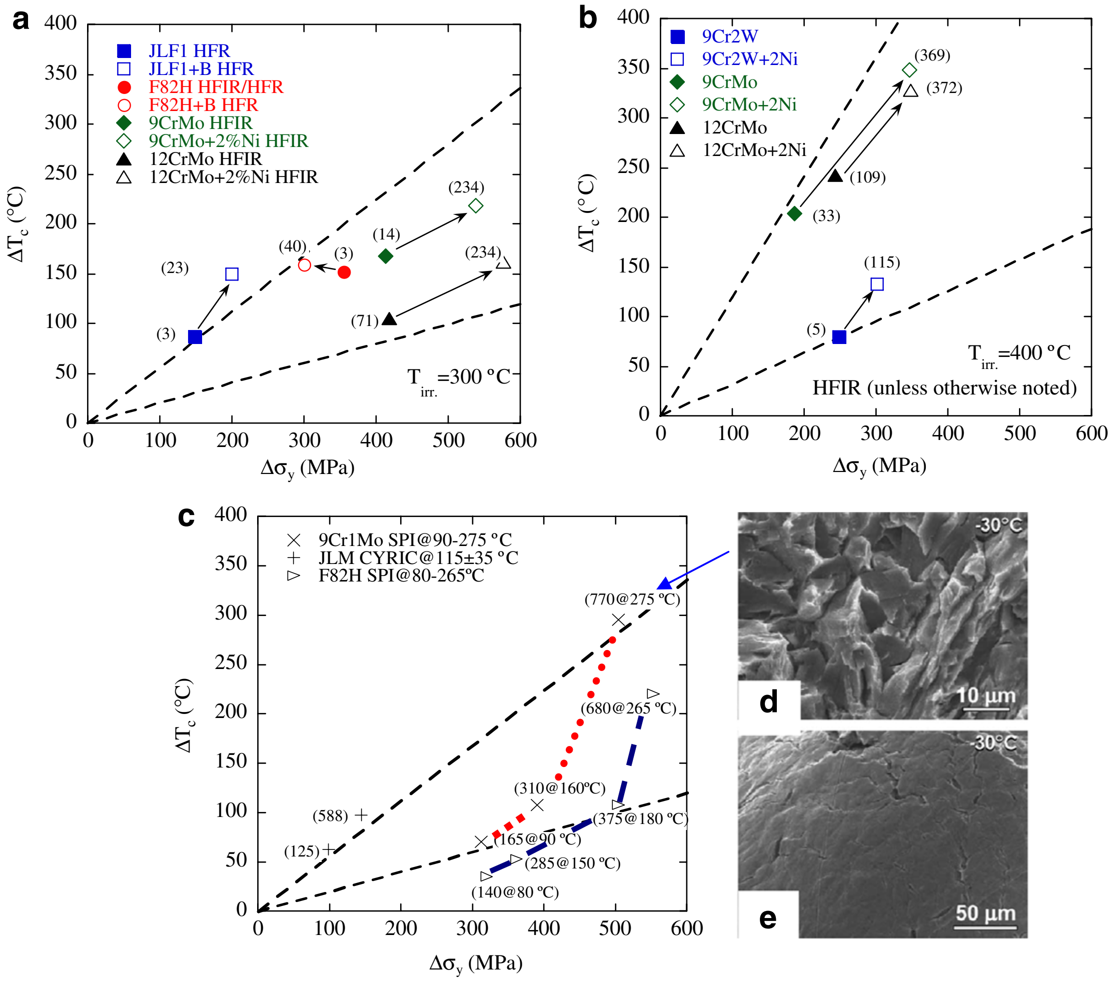

Fig. 13. (a) and (b) The ΔT_c versus $\Delta\sigma_y$ for data with helium variations due to B or Ni-doping in otherwise in nominally similar steels irradiated at (a) 300 °C; and (b) 400 °C. (c) SP irradiation small punch test ΔT_{sp} versus $\Delta\sigma_{yp}$ data with corresponding helium variations. (d) The fracture surface and (e) the bottom surface of punch-tested specimen with 770 appm He at 9.4 dpa showing a dominance of IGF [taken from Ref. [12]].

spallation proton irradiations of 9Cr1Mo T91 and F82H steels at nominal temperatures between ≈80 and 275 °C from ≈2.5 to 9.4 dpa producing ≈140 to 770 appm He [12,13]. Note the temperatures, He levels and dpa generally increase in tandem. Fig. 13(c) plots the small punch $\Delta T_c^{(sp)}$ versus $\Delta\sigma_{yp}$ data. The helium levels and nominal irradiation temperatures are shown in the parenthesis near each data point. At the intermediate helium levels, the data fall in the lower region of the overall ΔT_c versus $\Delta\sigma_y$ scatter band for this irradiation temperature range shown by the dashed lines. Jia and Dai also noted the fact that these data fall in the general scatter band of ΔT versus dpa for neutron irradiations [13]. However, there is a distinct break in the $\Delta T_c^{(sp)}$ versus $\Delta\sigma_{yp}$ trend for the data points at 680 appm He in F82H and 770 appm He in T91. Although the corresponding C_{sp} values are neither particularly high nor anomalous, the onset of significant amounts of IGF are observed in these cases, suggesting the emergence of a NHE contribution at very high helium levels. Note, IGF is readily observed both on the fracture surfaces and as a network of grain boundary cracks on the bottom surface of the small punch disc as shown in the micrographs taken from Ref. [12] (Fig. 13(d) and (e)).

Of course, the SP-irradiation results based on small punch tests do not represent a single variable experiment, and interpretations of this data should be viewed with considerable caution. For example, high levels of hydrogen and other transmutation products may also play a role in the larger C_c observed at the highest spallation proton dose, confounding unambiguous conclusions about the effects of helium acting alone. Fig. 13(c) also shows $\Delta T_c^{(sp)}$ versus $\Delta\sigma_{ym}$ data for 36 MeV α-ion irradiations to 100 and 600 appm He at 115 ± 35 °C based on assessments of ΔT_{sp} and hardening evaluated using Vickers microhardness tests ($\Delta\sigma_{ym}$) [15]. In this case, the $\Delta T_c^{(sp)}$ versus $\Delta\sigma_{ym}$ data fell near the top of the general scatter-band, but there is essentially no effect of higher helium on the $\Delta T_c^{(sp)}$ versus $\Delta\sigma_{ym}$ relation.

Another useful source of paired ΔT_c–$\Delta\sigma_{yd}$ data has been developed by Schneider and co-workers on a variety of steels that 'happen to have' different natural boron contents [21,22,91,92]. The Schneider database includes mixed spectrum neutron irradiations from 0.2 to 2.4 dpa at temperatures between 250 and 450 °C that produce up to ≈120 appm helium. Based on empirical plots of ΔT_c versus helium for subsets of this database, various authors [20,23] have also suggested a dominant role of helium on embrittlement. Indeed, fits to the overall database for $T_i < 400$ °C do result in a weak correlation that would indicate a strong effect of helium, that would, if true, result in an enormous $\Delta T_c \approx 1080$ °C at 1000 appm He. Note, the 450 °C data indicates that ΔT_c decreases with increasing helium, but is excluded from this analysis, since the C_c are very scattered and, as expected, are on average systematically larger than those observed at lower irradiation temperatures, indicating a NHE mechanism that is *not* related to helium. This is consistent with other observations of increased C_c at higher irradiation temperatures, but is not pertinent to the assessment of NHE due to helium. Even restricting the analysis to 400 °C or less, the ΔT_c versus helium data is very scattered and the statistical significance of the apparent correlation is low, with $r^2 \approx 0.21$.

However, a much more significant shortcoming of this sort of analysis is that it neglects the large range of $\Delta\sigma_{yd}$ in the irradiated steels. This masks the combined effects of both differences in dose (dpa) as well as the wide range of metallurgical variables representing the various alloys in the Schneider database. Both $\Delta\sigma_y$ and $C_c = \Delta T_c/\Delta\sigma_y$ (here, the dynamic yield stress increase) hence the corresponding ΔT_c, depend on these variables, in a way that is largely independent of either the alloy boron or helium content. Note, C_c itself also increases with $\Delta\sigma_y$ and depends on the alloy microstructure and unirradiated Charpy properties [5]. At lower irradiation temperatures, $\Delta\sigma_y$ is the most significant factor in controlling ΔT_c, thus it must be accounted for *before* attempting to evaluate any potential effects of any other variables.

Notably, three of the alloys with the highest boron contents in the Schneider database also contained significant quantities of nickel (0.66–0.92% Ni). At 300 °C, the $\Delta\sigma_{yd}$ in these nickel-bearing alloys is higher by an overall average factor of $\approx 1.6 \pm 0.25$ relative to a set of nominally similar nickel free alloys. Indeed, there is a systematic overall correlation between $\Delta\sigma_y$ and the alloy nickel content. The nickel sensitivity of $\Delta\sigma_y$ decreases with increasing T_i, dropping significantly between 350 and 400 °C. Fig. 14(a) shows that the ΔT_c versus $\Delta\sigma_y$ generally fall in the same scatter band as the larger overall database for ≈8Cr TMS, as shown by the dashed lines. Fig. 14(b) plots the corresponding $C_c = \Delta T_c/\Delta\sigma_y$ as a function of helium content. Least squares fits show an apparent effect of higher helium increasing ΔT_c only for the data for irradiations at 250 °C; and in that case, the effect of helium is primarily manifested in the range below 50 appm He, so is not very credible. The fits for the largest set of data for irradiations at 300 °C show only a very weak apparent effect of helium, while at higher temperatures there is a negative association between helium and C_c. A best fit to all the C_c data in the Schneider database for irradiations at $T_i \leqslant 400$ °C shown by the solid line, indicates a very weak, statistically insignificant, negative effect of helium. These results are not surprising, since all but one data point is below 100 appm helium. The scatter in $C_c = 0.41 \pm 0.2$ °C/MPa, shown by the horizontal dashed lines, is very consistent with the corresponding values for the larger overall TMS alloy database.

The band bounded by the short dashed lines on Fig. 14(c) represent the general scatter plot for the C_c found in the previous analysis, indicating no, or a weak, effect of helium up to ≈350 appm. Fig. 14(c) also shows the relation between C_{sp} and helium for the SP irradiation test data from Dai and Kasada as heavy dashed lines [12,15] normalized to a typical value of 0.4 °C/MPa at lower helium levels. The normalized C_c for the small punch test data exceed 1 °C/MPa at the highest helium level, consistent with a significant NHE of helium and the observation of IGF.

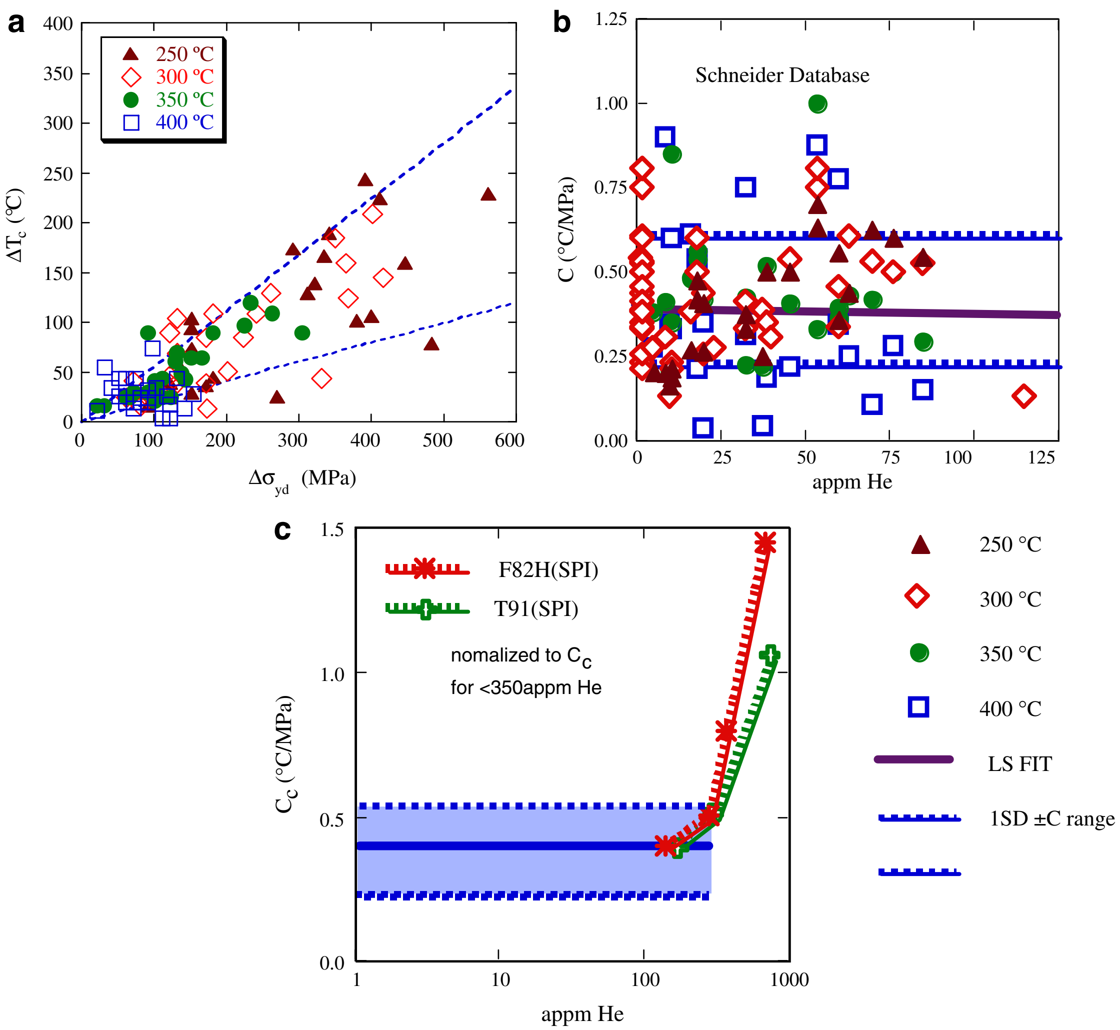

Fig. 14. (a) ΔT versus $\Delta\sigma_{yd}$ from Schneider's database compared to the overall scatter band for TMS irradiations at ⩽400; (b) $C_c = \Delta T_c/\Delta\sigma_{yd}$ for Schneider's database as a function of helium content with a least squares fit line; (c) C_c values from Schneider database along with paired lower-higher helium C_c values from Fig. 8(a) and (b) shown as heavy solid lines.

Another data set published by Henry and coworkers [10], at least indirectly pertinent to the issue of NHE, are the results of tensile tests at 25 and 250 °C following SP irradiations of a 9Cr1Mo (EM10) steel in various thermo-mechanical treatment conditions at ≈260 °C to ≈9.8 dpa and 750 appm He. The alloy conditions included as-tempered (AT), as-quenched (AQ) and tempered and cold-worked (CW). A strong effect of the alloy thermo-mechanical treatment and test temperature was observed in this dataset. In three cases the specimens failed after considerable deformation at reductions in area (RA) from about 44% to 48% that were somewhat less than the corresponding RA of 58–68% in the unirradiated condition. The RA ductility varied with test temperature and thermo-mechanical treatment condition and increased with decreasing σ_y (given in the parenthesis) in the order AT at 250 °C (960 MPa); AT at 25 °C (1150 MPa) and CW at 25 °C (1220 MPa). The fracture surfaces were a mixture of ductile microvoid coalescence and cleavage, with some IGF and transverse cracking. Assuming there is no strain hardening, the average fracture stress in the necked region is on the order of ≈2000 MPa, consistent with typical values of σ_c^* for cleavage. Indeed, the principal tri-axial stress would be even higher in the necked region, and this may compensate for some level of strain softening. The AQ alloy tested at 25 °C had the largest σ_y of 1320 MPa and lowest ductility with a RA of only 2% and ≈100% IGF. Given the small amount of necking prior to fracture it is not unreasonable to assume that $\sigma^*_{ig} = \sigma_y \approx 1300$ MPa, which is much lower than typical values of σ^*_c. This low value may at least in part be due to the high level of helium. This conclusion is supported by the observation that the fracture mode was ≈100% ductile microvoid coalescence after neutron irradiations of the AQ alloy to a slightly higher strength $\sigma_y \approx 1330$ MPa. A comparison of the fracture surfaces for the neutron and spallation proton irradiations is shown in Fig. 15 [10,19].

Jung and co-workers [14] have reported the results of tensile tests at 25 and 250 °C on EM10 and T91 after high-energy α-implantation at 250 °C to 0.8 dpa and 5000 appm He. These irradiations result in high $\sigma_y = 1079$ to 1217 MPa accompanied by very low ductility with the reduction in area (RA) ≈0% along with ≈100% IGF. The ductility was much higher and the σ_y much lower after α-implantations at 550 °C. The RA was also much lower for T91 tensile tests at 550 °C compared to 25 °C.

While no firm conclusions can be drawn from the tensile data, it is extremely significant that ≈100% IGF is observed at normal stress levels in the range of ≈1100 MPa (5000 appm He) to 1300 MPa (750 appm He). Further the results suggest that in addition to helium itself, NHE and IGF also depend on both the irradiation and test temperatures. Of course the presence of cracks or notches and/or high loading rates would make materials that are brittle even in a static tensile test, even more so in normal static fracture tests as well as under dynamic loading conditions.

Based on the observation of an apparent helium enhanced $C_c = \Delta T_c/\Delta\sigma_y > 0.4$ °C/MPa it is reasonable to assume that the corresponding toughness reference temperature shift would also increase with high helium to $C_0 = \Delta T_0/\Delta\sigma_y > 0.6$ °C/MPa. In combination with the model for $\Delta\sigma_y(\mathrm{dpa}, T_i)$ as shown in Fig. 4, this hypothesis can be used to construct a simple model for ΔT_c and ΔT_0 as

$$\Delta T_{c/0} \approx C_{c/0}(\mathrm{He})\,\Delta\sigma_y(\mathrm{dpa},T_i). \tag{5}$$

Based on the normalized $C_{sp}(\mathrm{He})$ trends in Fig. 14(c), we crudely estimate the $C_{c/k}(\mathrm{He})$ as

$$C_{c/0}(\mathrm{He}) = (0.4 \text{ or } 0.6) + 0.0007(\mathrm{He} - 500)\ ^\circ\mathrm{C/MPa} \quad 500 \leqslant \mathrm{He} \leqslant 1500, \tag{6a}$$

$$C_{c/0}(\mathrm{He}) = 1.1 \text{ or } 1.3\ ^\circ\mathrm{C/MPa} \quad \mathrm{He} > 1500. \tag{6b}$$

Here we have taken the absolute rate of increase of C_{sp} with helium above the threshold; using the normalized value would increase the helium coefficient by about a factor of ≈2. Fig. 16 shows the resulting ΔT_0 and ΔT_c predictions for $T_i = 300$ °C for typical fusion reactor (Fig. 16(a), He/dpa = 10 appm/dpa) and SP irradiation (Fig. 16(b), He/dpa = 100 appm/dpa) environments. Fig. 16 also shows the additional effect of dynamic (ε'_d) versus static (ε'_s) loading rate on the total shift. The T_0 shift due to dynamic loading, ΔT_d, is given by a strain rate compensated temperature T_d which is higher than the equivalent static fracture temperature using the expression [104,105]

$$\Delta T_d = T_s\{[1 + 0.035\ln(\varepsilon'_d/\varepsilon'_s)] - 1\}. \tag{7}$$

The predicted shifts are large from hardening alone and become enormous at high He levels. Assuming a starting $T_{c/0}$ of −100 °C, the irradiated $T_{c/0/d}$

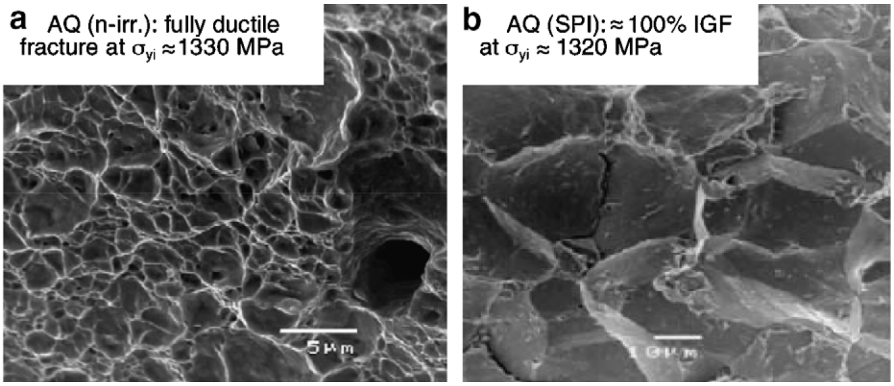

Fig. 15. Tensile fracture surfaces of an AQ 9CrMo steel after (a) neutron and (b) spallation proton irradiations to the similar levels of σ_y at ≈250 °C, showing ductile and IGF, respectively [from Refs. [10,19]].

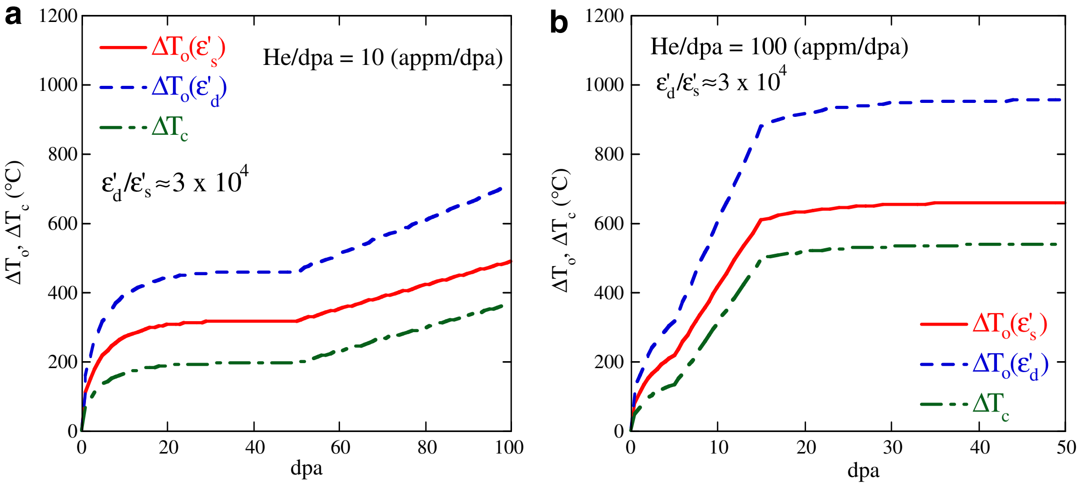

Fig. 16. Composite $C_{c/0/d}$(He) and $\Delta\sigma_y$(dpa) model predictions of ΔT_0, ΔT_c and ΔT_d (dynamic) for $T_i = 300$ °C for typical (a) fusion reactor (He/dpa = 10 appm/dpa); and (b) SP irradiation (He/dpa = 100 appm/dpa) environments.

quickly reach values in excess of the irradiation temperature (≈300 °C). Notably, $T_{0/d}$ values of 400 °C would result in unacceptable median toughness values of <40 MPa$\sqrt{}$m, as well as lower shelf bounding toughness. However, it is important to emphasize that these plots cannot be viewed as ‘predictions’, but rather they are meant to emphasize the potential importance of the synergistic high helium-high hardening effects.

4. Discussion, summary and conclusions

The work reported here on developing and analyzing a comprehensive database on irradiation effects on the mechanical properties of ≈8Cr TMS alloys should be viewed as a first step, work in progress in a long-term effort. However, the preliminary evaluation of the T_i and dpa-dependence of irradiation hardening, $\Delta\sigma_y$, and embrittlement, ΔT_c, has provided considerable insight that will help to guide future research. First, it is clear that the existing database is not sufficient. Future experiments must strive to avoid uncontrolled variables and confounding variable combinations, as well as to provide sufficient detail to be compatible with inclusion in a high quality database. Such details should include explicit estimates of uncertainties in key parameters, such as the irradiation temperature, T_i.

In spite of the limitations in the database, however, our analysis provided a first-iteration semi-empirical model of the dpa, T_i and T_t dependence of $\Delta\sigma_y$ and ΔT_c. This model will be refined in the future, but demonstrates that very large $\Delta\sigma_y$ approaching 500–600 MPa can be anticipated at high doses at T_i around 300 °C, especially at lower T_t. There appears to be little systematic difference between hardening produced by spallation proton (SP) and neutron irradiations with very high and low He/dpa ratios, respectively. Our analysis also shows that neutron irradiation embrittlement is dominated by hardening below $T_i \approx 400$ °C for helium levels up to ≈400 appm. However, the hardening-shift coefficient, $C_c = \Delta T_c/\Delta\sigma_y$, for sub-sized Charpy tests, is lower than for fracture toughness reference temperature shifts, ΔT_0. Thus ΔT_c is a *non-conservative* measure of embrittlement. Clearly, future irradiation experiments must focus on establishing a comprehensive ΔT_0 database as well as for other fracture toughness properties, like ductile tearing resistance.

Our analysis also suggests that a non-hardening embrittlement (NHE) contribution to ΔT_c occurs at $T_i > 400$ °C. The NHE can be rationalized on the basis of decreases in thermal aging temperatures due to radiation enhanced diffusion (RED), typically occurring at temperatures >500 °C. While probably not a major issue per se, such NHE may act synergistically with hardening and other NHE mechanisms, such as those due to high concentration of and helium and possibly hydrogen.

We have collected and analyzed a variety of data pertinent to the issue of the effect of helium on fast fracture by evaluating the relation between ΔT_c and

$\Delta\sigma_y$. The hardening-shift relation was assessed both in terms of ΔT_c versus $\Delta\sigma_y$ scatter plots and trends in $C_c = \Delta\ T_c/\Delta\sigma_y$. Large values of C_c, as well as transition from TGC to IGF, at high helium concentrations were used as signatures of possible NHE due to helium. While the data is scattered, and to some degree confounded by uncontrolled variables, the results suggest that up to concentrations several hundred appm, helium has little effect on C_c or ΔT_c. However, at higher concentrations generated in SP and HI irradiations, the data is consistent with the hypothesis that accumulation of helium sufficiently weakens grain boundaries to the point where a NHE effect emerges as signaled by both higher C_c and IGF. This hypothesis is also supported by the results of tensile tests on TMS in both high strength irradiated state and implanted with very high concentrations of helium. Notably, previous fractography studies to characterize IGF have been very limited and should be a major focus of future work.

Acknowledgements

The authors explicitly acknowledge the extensive research that produced the data analyzed in this paper and thank the researchers cited in the references for their major contributions to the development of materials for fusion reactors. Our many fruitful collaborations with many US colleagues in the Advanced (Fusion) Materials program, Philippe Spätig of EPFL-CRPP and Yong Dai of PSI are also gratefully acknowledged. The work described here was supported by the US Department of Energy, Office of Fusion Science (DE-FG03-94ER-5475).

References

[1] G.R. Odette, T. Yamamoto, H.J. Rathbun, M.Y. He, M.L. Hribernik, J.W. Rensman, J. Nucl. Mater. 323 (2003) 313.

[2] G.R. Odette, B.D. Wirth, D.J. Bacon, N.M. Ghoniem, MRS Bull. (2001) 176.

[3] S. Jumel, C. Domain, J. Ruste, J.-C. Van Duysen, C. Becquart, A. Legris, P. Pareige, A. Barbu, E. Van Walle, R. Chaouadi, M. Hou, G.R. Odette, R.E. Stoller, B.D. Wirth, J. Test. Eval. 30-1 (2002) 37.

[4] K. Shiba, A. Hishinuma, A. Toyama, K. Masamura, Properties of the reduced activation ferritic steel F82H IEA heat, JAERI-Tech 97-038 (1997) (in Japanese).

[5] K. Shiba, M. Suzuki, A. Hishinuma, J. Nucl. Mater. 233–237 (1996) 309.

[6] H.E. Hofmans, Tensile and impact properties of Eurofer97 plate and Bar, NRG Petten 200023/00.38153/P.

[7] J. Rensman, H.E. Hofmans, E.W. Schuring, J. van Hoepen, J.B.M. Bakker, R. den Boef, F.P. van den Broek, E.D.L. van Essen, J. Nucl. Mater. 307–311 (2002) 250.

[8] J.-W. Rensman, NRG irradiation testing: report on 300 °C and 60 °C irradiated RAFM steels, NRG Petten 20023/05.68497/P.

[9] K. Farrell, T.S. Byun, J. Nucl. Mater. 296 (2001) 129.

[10] J. Henry, X. Averty, Y. Dai, P. Lamagnére, J.P. Pizzanelli, J.J. Espinas, P. Wident, J. Nucl. Mater. 318 (2003) 215.

[11] S.A. Maloy, M.R. James, G. Willcutt, W.F. Sommer, M. Sokolov, L.L. Snead, M.L. Hamilton, F. Garner, J. Nucl. Mater. 296 (2001) 119.

[12] Y. Dai, X.J. Jia, K. Farrell, J. Nucl. Mater. 318 (2003) 192.

[13] X. Jia, Y. Dai, J. Nucl. Mater. 323 (2003) 360.

[14] P. Jung, J. Henry, J. Chen, J.-C. Brachet, J. Nucl. Mater. 318 (2003) 241.

[15] R. Kasada, T. Morimura, A. Hasegawa, A. Kimura, J. Nucl. Mater. 299 (2001) 83.

[16] P. Jung, C. Liu, J. Chen, J. Nucl. Mater. 296 (2001) 165.

[17] A. Kimura, R. Kasada, K. Morishita, R. Sugano, A. Hasegawa, K. Abe, T. Yamamoto, H. Matsui, N. Yoshida, B.D. Wirth, T.D. Rubia, J. Nucl. Mater. 307–311 (2002) 521.

[18] A. Hasegawa, H. Shiraishi, H. Matsui, K. Abe, J. Nucl. Mater. 212–215 (1994) 720.

[19] J. Henry, M.-H. Mathon, P. Jung, J. Nucl. Mater. 318 (2003) 249.

[20] M. Rieth, B. Dafferner, H.-D. Rohrig, J. Nucl. Mater. 258–263 (1998) 1147.

[21] H.-C. Schneider, B. Dafferner, J. Aktaa, J. Nucl. Mater. 295 (2001) 16.

[22] H.-C. Schneider, B. Dafferner, J. Aktaa, J. Nucl. Mater. 321 (2003) 135.

[23] R. Lindau, A. Möslang, D. Preininger, M. Rieth, H.D. Röhrig, J. Nucl. Mater. 271&272 (1999) 450.

[24] B. Van der Schaaf, D.S. Gelles, S. Jitsukawa, A. Kimura, R.L. Klueh, A. Möslang, G.R. Odette, J. Nucl. Mater. 283–287 (2000) 52.

[25] B. Van der Schaaf, A.A. Tavasoli, Hardening and toughness from radiation and resistance characterization of F82H and screening steels, NRG Petten 20027/99.25387/P.

[26] R.L. Klueh, D.J. Alexander, J. Nucl. Mater. 187 (1992) 60.

[27] R.L. Klueh, D.J. Alexander, J. Nucl. Mater. 218 (1995) 151.

[28] R.L. Klueh, D.S. Gelles, S. Jitsukawa, A. Kimura, G.R. Odette, B. van der Schaaf, M. Victoria, J. Nucl. Mater. 307–311 (2002) 455.

[29] E. Lucon, Mechanical properties of the European reference RAFM steel (Eurofer97) before and after irradiation at 300 °C (0.3–2 dpa), SCKCEN Report BLG-962, November 2003, Mol, Belgium.

[30] M.J. Makin, A.D. Whapham, F.J. Minter, Philos. Mag. 7 (74) (1962) 285.

[31] M.J. Makin, F.J. Minter, Acta Metall. Mater. 8 (10) (1960) 691.

[32] A. Kimura, T. Morimura, M. Narui, H. Matsui, J. Nucl. Mater. 233–237 (1996) 319.

[33] R. Kasada, A. Kimura, H. Matsui, M. Narui, J. Nucl. Mater. 258–263 (1998) 1199.

[34] P. Spätig, R. Schaublin, S. Gyger, M. Victoria, J. Nucl. Mater. 258–263 (1998) 1345.

[35] R. Kasada, A. Kimura, H. Matsui, A. Hasegawa, M. Narui, J. Nucl. Mater. 271–272 (1999) 360.

[36] Y. Dai, S.A. Maloy, G.S. Bauer, W.F. Sommer, J. Nucl. Mater. 283–287 (2000) 513.

[37] E.V. van Osch, J.V. van Hoepen, J. Boskeljon, J. Rensman, Tensile properties of 2.5 dpa 300 °C neutron irradiated RA FM plate, powder HIP and EB and TIG weld, NRG Petten 20023/99.26704/P.

[38] R.L. Klueh, J. Alexander, ASTM STP 1325 (1999) 911.

[39] E.I. Materna-Morris, H.-C. Schneider, B. Dafferner, R. Rolli, O. Romer, Irradiation influences on mechanical properties and structures of martensitic low-activation alloys, Presented in ICFRM-10.

[40] K. Shiba, personal communication.

[41] H. Kurishita, H. Kayano, M. Narui, A. Kimura, M.L. Hamilton, D.S. Gelles, J. Nucl. Mater. 212–215 (1994) 730.

[42] F. Abe, T. Noda, H. Araki, M. Narui, H. Kayano, J. Nucl. Mater. 191–194 (1992) 845.

[43] R.L. Klueh, P.J. Maziasz, M. Vitek, J. Nucl. Mater. 141–143 (1986) 960.

[44] A. Kohyama, H. Matsui, K. Hamada, H. Simidzu, J. Nucl. Mater. 155–157 (1988) 896.

[45] R.L. Klueh, J. Nucl. Mater. 179–181 (1991) 728.

[46] R.L. Klueh, J.M. Vitek, M.L. Grossbeck, ASTM STP 782 (1982) 648.

[47] J. Russell Hawthorne, J.R. Reeds, J.A. Sprague, ASTM STP 870 (1985) 580.

[48] K. Farrell, T.S. Byun, J. Nucl. Mater. 318 (2003) 274.

[49] V.K. Shamardin, V.N. Golovanov, T.M. Bulanova, A.V. Povstyanko, A.E. Fedoseev, Z.E. Ostrovsky, Yu.D. Goncharenko, J. Nucl. Mater. 307–311 (2003) 229.

[50] V.V. Rybin, I.P. Kursevich, A.N. Lapin, J. Nucl. Mater. 258–263 (1998) 1324.

[51] A. Alamo, M. Horsten, X. Averty, E.I. Materna-Morris, M. Rieth, J.C. Brachet, J. Nucl. Mater. 283–287 (2000) 353.

[52] R.L. Klueh, M. Sokolov, K. Shiba, Y. Miwa, J.P. Robertson, J. Nucl. Mater. 283–287 (2000) 478.

[53] R.L. Klueh, J.J. Kai, D.J. Alexander, J. Nucl. Mater. 225 (1995) 175.

[54] E.I. Materna-Morris, M. Rieth, K. Ehrlich, Effects of radiation on materials, in: 19th International Symposium, ASTM STP 1366 (2001) 597.

[55] E.V. van Osch, M.G. Horsten, G.E. Lucas, G.R. Odette, Effects of radiation on materials, in: 19th International Symposium, ASTM STP 1366 (2001) 612.

[56] J. Rensman, J. van Hoepen, J.B.M. Bakker, R. den Boef, F.P. van den Broek, E.D.L. van Essen, J. Nucl. Mater. 307–311 (2002) 245.

[57] J.L. Séran, A. Alamo, A. Maillard, H. Touron, J.C. Brachet, P. Dubuission, O. Rabouille, J. Nucl. Mater. 212–215 (1994) 588.

[58] M.A. Sokolov, R.L. Klueh, G.R. Odette, K. Shiba, H. Tanigawa, ASTM STP 1447 (2004) 408.

[59] A. Alamo, V. Lambard, X. Averty, M.H. Mathon, J. Nucl. Mater. 329–333 (2004) 333.

[60] E. Lucon, R. Chaouadi, M. Decreton, J. Nucl. Mater. 329–333 (2004) 1078.

[61] E. Wakai, T. Taguchi, T. Yamamoto, F. Takada, J. Nucl. Mater. 329–333 (2004) 1133.

[62] C. Liu, H. Klein, P. Jung, J. Nucl. Mater. 335 (2004) 77.

[63] N. Baluc, R. Schaublin, P. Spätig, M. Victoria, ASTM STP 1447 (2004) 341.

[64] A. Kimura, Fusion Sci. Technol. 44 (2) (2003) 480.

[65] Y. Kohno, A. Kohyama, T. Hirose, M.L. Hamilton, M. Narui, J. Nucl. Mater. 271&272 (1999) 145.

[66] R.L. Klueh, J. Nucl. Mater. 132 (1989) 13.

[67] E.D. Eason, J.E. Wright, G.R. Odette, NUREG/CR-6551, US NRC, Washington DC, 1998.

[68] G.R. Odette, T. Yamamoto, D. Klingensmith, H. Kishimoto, UCSB-NRC-03/2, 2003.

[69] R.B. Jones, T.J. Williams, ASTM STP 1270 (1996) 569.

[70] R.L. Klueh, P.J. Maziasz, J. Nucl. Mater. 187 (1992) 43.

[71] J.L. Séran, V. Lévy, P. Dubisson, D. Gilbon, A. Maillard, A. Fissolo, H. Touron, R. Cauvin, A. Chalony, E. Le Boulbin, ASTM STP1125 (1992) 1209.

[72] G.R. Odette, P.M. Lombrozo, R.A. Wullaert, ASTM STP 870 (1985) 841.

[73] G.R. Odette, M.Y. He, J. Nucl. Mater. 283–287 (2000) 120.

[74] L. Schäfer, J. Nucl. Mater. 283–287 (2000) 707.

[75] H. Sakasegawa, T. Hirose, A. Kohyama, Y. Katoh, T. Harada, K. Asakura, T. Kumagai, J. Nucl. Mater. 307–311 (2002) 490.

[76] L.K. Mansur, J. Nucl. Mater. 318 (2003) 14.

[77] G.R. Odette, G.E. Lucas, Radiat. Eff. Def. 144 (1998) 189.

[78] G.R. Odette, G.E. Lucas, D. Klingensmith, B.D. Wirth, D. Gragg, NUREG/CR-6778, 2002.

[79] G.R. Odette, T. Yamamoto, D. Klingensmith, Philos. Mag. 85 (2005) 779.

[80] D.S. Gelles, G.L. Hankin, M.L. Hamilton, J. Nucl. Mater. 251 (1997) 188.

[81] N. Hashimoto, R.L. Klueh, J. Nucl. Mater. 305 (2002) 153.

[82] R.L. Klueh, D.J. Alexander, J. Nucl. Mater. 233–237 (1996) 336.

[83] I.V. Gorynin, V.V. Rybin, I.P. Kursevich, A.N. Lapin, E.V. Nesterova, E.Yu. Klepikov, J. Nucl. Mater. 283–287 (2000) 465.

[84] N. Baluc, R. Schaublin, C. Bailat, F. Paschoud, M. Victoria, J. Nucl. Mater. 283–287 (2000) 731.

[85] R.L. Klueh, D.J. Alexander, M. Rieth, J. Nucl. Mater. 273 (1999) 146.

[86] E.V. van Osch, J.B.M. Bakker, R. den Boef, J. Rensman, NRG Petten 20023/99.26974/P.

[87] R.L. Klueh, D.J. Alexander, J. Nucl. Mater. 258–263 (1998) 1269.

[88] T. Lechtenberg, J. Nucl. Mater. 133&134 (1985) 149.

[89] R.L. Klueh, J.M. Vitek, W.R. Corwin, D.J. Alexander, J. Nucl. Mater. 155–157 (1988) 973.

[90] H. Kayano, A. Kimura, M. Narui, Y. Sasaki, Y. Suzuki, S. Ohta, J. Nucl. Mater. 155–157 (1988) 978.

[91] R.L. Klueh, D.J. Alexander, J. Nucl. Mater. 179–181 (1991) 733.

[92] W.L. Hu, D.S. Gelles, ASTM STP 956 (1987) 83.

[93] H.-C. Schneider, B. Dafferner, H. Ries, O. Romer, Irradiation program MANITU: results of impact tests with the irradiated materials (2.4 dpa), FZKA6605, Forschungszentrum Karlsruhe, 2001.

[94] H.-C. Schneider, B. Dafferner, H. Ries, S. Lautensack, O. Romer, Irradiation programme HFR phase 1b: results of impact tests with the irradiated materials (2.4 dpa), FZKA 6976, Forschungszentrum Karlsruhe, 2004.

[95] R.L. Klueh, J.M. Vitek, J. Nucl. Mater. 132 (1985) 27.

[96] E. Lucon, M. Decréton, E. van Walle, Fusion Eng. Des. 69 (2003) 373.

[97] A. Kimura, H. Kayano, M. Narui, J. Nucl. Mater. (1991) 737.

[98] C. Liu, H. Klein, P. Jung, J. Nucl. Mater. 335 (2004) 77.
[99] P. Fernandez, A.M. Lancha, J. Lapena, M. Hernandez-Mayoral, Fusion Eng. Des. 58–59 (2001) 787.
[100] Y. Ruan, P. Spaetig, M. Victoria, J. Nucl. Mater. 307–311 (2003) 236.
[101] J. Kameda, X. Mao, J. Mater. Sci. 27 (1992) 983.
[102] R.L. Klueh, J.M. Vitek, J. Nucl. Mater. 150 (1987) 272.
[103] S. Jitsukawa, A. Kimura, A. Kohyama, R.L. Klueh, A.A. Tavassoli, B. van der Schaaf, G.R. Odette, J.W. Rensman, M. Victoria, C. Petersen, J. Nucl. Mater. 329–333 (2004) 39.
[104] P. Spätig, G.R. Odette, E.G. Donahue, G.E. Lucas, J. Nucl. Mater. 283–287 (2000) 721.
[105] E.G. Donahue, G.R. Odette, G.E. Lucas, J. Nucl. Mater. 283–287 (2000) 637.